DILUTE NON-NEWTONIAN PARTICLE SUSPENSION RHEOLOGY AND MICROSTRUCTURE

A Dissertation

Presented to the Faculty of the Graduate School

of Cornell University

in Partial Fulfillment of the Requirements for the Degree of

Doctor of Philosophy

by

Eric F. Lee

February 2010

DILUTE NON-NEWTONIAN PARTICLE SUSPENSION RHEOLOGY AND MICROSTRUCTURE

Eric F. Lee, Ph.D.

Cornell University 2010

The study of polymeric particle suspensions has been the subject of a number of past experimental and theoretical studies. However, fundamental questions about suspension rheology and shear flow-induced microstructural effects remain. First, a quasi-analytical study is presented that gives the first theory-based predictions on the effects of finite polymer relaxation time on rheological properties. In a constant viscosity, low polymer concentration fluid, the addition of particles is found to have a strong shear thickening effect on the first normal stress difference coefficient and the shear viscosity. In contrast, the second normal stress difference coefficient is shear thickening at low shear but shear thinning at higher shear. Next, an analytical and computational study is presented that sheds light on the widely studied phenomenon of cross-streamline particle migration in Poiseuille flow. Particles are found to experience a cross-stream force toward the channel center when they are freely suspended in the fluid, while they experience a cross-stream force toward the wall when they are fixed in place.

BIOGRAPHICAL SKETCH

Eric Lee was born and raised in Lenoir City, Tennessee, where his parents still reside. He graduated from Webb School in Knoxville, and then attended Rice University, where he graduated with a B. S. in Chemical Engineering and a B. A. in Mechanical Engineering in 2003. Afterward, he joined the chemical engineering program at Cornell.

ACKNOWLEDGEMENTS

I first want to thank my advisors, Professors Don Koch, Yong Joo, and Lynden Archer. I am indebted to them for their guidance in my research.

I want to thank my family–my parents Don and Sandra and my brother Andy. My parents have always inspired me and will continue to do so. Their encouragement and support has been unyielding through my whole life. My brother has always been my best friend, and he understands me probably more than anyone else does.

I would like to thank Prof. Abe Stroock. Serving as a TA for him, I learned a great deal about teaching effectively and am happy to have participated in the many discussions about the class, where Abe never lost track of his goal to inspire the students to be creative engineers. Linda Tompkins and the rest of the TA Training staff were also great, and I think that they definitely helped me gain a lot of enthusiasm for teaching as a passion.

I would like to thank my research group for their help, especially Brian Pasquini for giving me many tips from his vast knowledge of Linux expertise.

Thanks to all of my many housemates that I've had at Stewart Little. I will really miss the house, the dinners, and the good times. I also want to thank my friends that I have met here in Ithaca, who I will be sorry to have to leave.

My time at Cornell has been a good one, and I will definitely carry great memories with me. I am nevertheless eager to move to the next step. So, with this, I say farewell. It has been great!

TABLE OF CONTENTS

LIST OF TABLES

LIST OF FIGURES

LIST OF SYMBOLS

a	Particle radius
A	Area
$\boldsymbol{A}$	Polymer conformation tensor
A_{ijk}	$\frac{1}{2}\left(\frac{\partial U_i}{\partial x_j \partial x_k}\right)$
c	Polymer concentration
d	Distance from the wall to the particle center
De	Deborah number ($\lambda_r \dot{\gamma}$)
$\boldsymbol{e}$	Rate of strain
$\boldsymbol{F}$	Force
h	The value of X_2 at the cylinder surface, $1 + X_1^2/2$
H	Height of channel
n	Number of particles per volume
$\boldsymbol{n}$	Unit normal vector
p	Pressure
r	Radial coordinate
$\boldsymbol{r}$, $\boldsymbol{x}$	Position in Cartesian coordinates
$\boldsymbol{S}$	Stresslet
t	Time
u	Fluid velocity
U_{max}	Maximum velocity of undisturbed Poiseuille flow
$\boldsymbol{v}$	Particle velocity
V	Volume
X_1	$x_1/\epsilon^{1/2}$
X_2	$(x_2 + d)/\epsilon$
Z_1, Z_2	Fourier transform constants
β	η_S/η_0
ϵ	Non-dimensional gap thickness
η_0	Zero shear viscosity
η_s	Solvent viscosity
$\dot{\gamma}$	Shear rate
κ	Non-dimensional particle size (a/H)
λ	Non-dimensional particle location (d/H)
λ_r	Polymer relaxation time
ω	Particle rotation speed
$\boldsymbol{\omega}$	Vorticity
ϕ	Particle volume fraction, angle in spherical coordinates
Π	Polymer stress
ψ_1, ψ_2	First and second normal stress difference coefficients
$\boldsymbol{\sigma}$	Fluid Stress
$\boldsymbol{\tau}$	Newtonian stress
θ	Angle

Chapter 1

Introduction

Particle suspensions have been extensively studied, in part due to the large number and varied nature of applications in which they are employed, including the areas of food processing, cosmetics, and biomedical materials. The reasons that manufacturers add polymers and particles to solutions are many. The addition of polymers can improve solution stability as well as change the aesthetics of the resultant solution, making it "thicker or creamier" [1]. The addition of particles can be useful for a variety of reasons, including applications where abrasive properties (e. g. toothpaste) or scratch-resistance (e. g. car paint) are important. The addition of polymers and particles leads to a change in the bulk stresses of the solution, and these additional non-isotropic stresses may require the manufacturer to change the industrial process. Examples of possible changes include a different bottling process due to die swell at the exit of a pipe or larger pumps to drive the solution through the piping. Microstructural effects are also a concern for manufacturers, as they can cause inhomogeneities in the suspension. These effects can be partly controlled by processing methods, as different imposed flow fields give different resultant suspension microstuctures. Inhomogeneities can be beneficial or detrimental to different products, depending on the desired properties of the processed suspension. Flow time is an important processing concern, as longer flow times lead to more inhomogeneities.

Thus, the challenges of describing the material properties of suspensions are many, and they lead to some of the exciting unresolved problems that researchers in the field are currently tackling. As suspensions display a range of behaviors based on the physical and chemical properties of the particles and the suspending fluid, no

theory fully describes their rheology. This thesis considers rigid, neutrally buoyant particles in the dilute limit (low particle concentration) where particle-particle interactions are negligible. It neglects any particle-fluid chemical interactions, thus considering effects solely derived from the rheological properties of the suspending fluid and the choice of bulk flow field. It examines non-Newtonian suspending fluids in the creeping flow limit, where inertial effects are negligible. The results apply for particle sizes that are large enough that Brownian motion is negligible and small enough that the creeping flow limit is satisfied.

The challenge of obtaining flow field solutions for a particle suspension in viscoelastic shear flow combines the complexities associated with flow modifications due to the presence of both 1) suspended particles and 2) polymers. The effects of the addition of each of these modifiers to the flow field and appropriate flow field solution techniques will briefly be introduced before discussing the specifics of the overall problems that are investigated in this thesis.

1.0.1 Particle suspensions

Einstein did some of the first work in the field of particle suspensions, finding that the relative viscosity $\eta_r = \eta/\eta_0$ of a suspension was related to the particle volume fraction ϕ by the simple expression $\eta_r = 1 + \frac{5}{2}\phi$. Here, η is the viscosity for the suspension at a given particle volume fraction and η_0 is the zero shear rate viscosity of the suspending fluid. Since this equation was developed, researchers have further developed Einstein's theory by considering the effects of high particle concentration [3], Brownian motion [2], particle-particle non-hydrodynamic interactions [22], particle-fluid non-hydrodynamic interactions [1], and particle shape [20] on the suspension viscosity. In addition to the bulk fluid viscosity change,

Einstein found that the addition of particles gives rise to an extra stress in the suspension. This extra stress, called a stresslet, is proportional to the first power of the particle concentration in the dilute limit, given as $\frac{20}{3}\pi\phi\boldsymbol{E}$, where $\boldsymbol{E}$ is the mean rate of strain in the suspension.

In order to determine the flow field around a particle, the Newtonian velocity and pressure fields for an imposed shear flow are found by performing a multipole expansion of the fluid velocity and pressure fields. A torque-free, force-free boundary condition is applied on the particle surface. In the study of particle migration outlined in Chapter 3, the flow field equations are complicated by additional flows that must be superpositioned on top of this bulk shear flow in order to accurately write the equations for a migrating particle or a stationary particle. With the solutions to these Newtonian equations, the constitutive equations outlined in the following section can be solved either analytically or numerically, depending on the mathematical complexity of the constitutive model.

1.0.2 Polymer rheology

Polymer solutions have a variety of unique properties and can be labeled as a class of materials that lie somewhere in between ordinary liquids and solids. They are described as "viscoelastic" because they can flow like viscous liquids and deform like elastic solids, with properties ranging from completely viscous to completely elastic behavior. Some factors affecting how viscous or how elastic the solution is include the choice of polymer species, the choice of solvent, the particle concentration, and external properties such as the flow geometry and the temperature.

Often the first property that is considered when examining a polymeric fluid is

how the viscosity changes based on shear rate. Polymeric liquids display a range of behaviors as the shear rate increases, from solutions that "thin", exhibiting a decrease in viscosity with increasing shear rate, to solutions that "thicken", exhibiting an increase in viscosity with increasing shear rate. Other key suspension properties that are studied are the first (N_1) and second (N_2) normal stress differences, defined as $N_1 = \sigma_{11} - \sigma_{22}$ and $N_2 = \sigma_{22} - \sigma_{33}$, where σ is the stress tensor, 1 is the direction of the flow, 2 is the direction of the velocity gradient, and 3 is the direction of the vorticity. Normal stress differences give rise to some of the unique elastic behaviors observed in polymeric solutions and are important in polymer suspension processing applications due to their effect on suspension microstructure. In elastic polymer solutions in simple shear flow, the polymers stretch along the elongational axis and thus cause the fluid to have a positive first normal stress difference [27] and a weaker negative second normal stress difference.

In this thesis, the second-order fluid and Oldroyd-B constitutive equations are used to describe the stress in the polymeric solution. Both of these constitutive equations are excellent for studying elastic effects and the resulting microstructural changes in the suspension. The second-order fluid stress is derived from a polynomial expansion involving powers of the rate of strain tensor and its convected derivative. Unlike most other complex fluid models, the second-order fluid model has the advantage of being analytically tractable. The primary limitations of the model are the requirements that the flows be slowly changing, such that the rate of strain tensor and vorticity tensor are small, and that the time derivatives of fluid quantities be small. These requirements are satisfied at low Deborah number (De), where De is defined as the ratio of the polymer relaxation time to the characteristic flow time (such as the inverse shear rate). As the second-order fluid accurately describes all fluids in the low De limit, it serves as a good model for

elastic effects in a viscoelastic fluid with a small polymer relaxation time. It is also very useful in giving physical insight into polymeric behaviors due to its relative mathematical simplicity. Lastly, it is useful in verifying (in the appropriate low De limit) and complementing computational results obtained with other constitutive models.

The Oldroyd-B fluid expands upon the idea of a second-order fluid by adding a convected time derivative of the stress tensor, thus allowing convection of both the rate of strain tensor and the fluid stress tensor. The constitutive model is derived from kinetic theory for a dilute polymer solution in a viscous Newtonian solvent, which can be replicated experimentally for a class of fluids known as Boger fluids. It is one of the most widely studied because it accurately predicts the viscoelastic behavior and the first normal stress difference for this class of fluids. It should be noted that the model has some limitations. First, the model gives a constant viscosity and first normal stress difference for all shear rates, thus not predicting the common effect of shear thinning seen in many polymeric solution. Also, the model gives no second normal stress difference; generally, real viscoelastic solutions have a negative second normal stress difference that is around an order of magnitude smaller than the first normal stress difference. Unlike the second-order fluid, the Oldroyd-B fluid can predict time-dependent behavior and thus eliminates the low De requirement. In addition to exploring higher De flows, the simulations using the Oldroyd-B equation allow us to examine complex flow configurations that cannot be determined analytically due to geometric or flow constraints.

The constitutive models introduced above relate the flow field to the stress field; thus, the Newtonian flow field solutions discussed in the previous section can be substituted into a constitutive model to give a prediction of the non-Newtonian suspension behavior, using appropriate theorems and/or numerical solutions. In

the case of the second-order fluid, the Tanner-Pipkin theorem states that the O(De) velocity field is the same as the Newtonian one, and for the Oldroyd-B fluid in the rheology study, we make use of the reciprocal theorem in order to avoid explicitly calculating the flow modification due to non-zero polymer concentration.

Having given a background in polymer suspension fluid mechanics, introductions to the specific investigations undertaken in this thesis are now presented. First, in order to understand the effects of finite polymer relaxation time on the bulk stress of a suspension, the rheology of spherical particles in a non-Newtonian suspension is studied. Second, one of the principal microstructural effects observed in polymer-particle suspensions—cross streamwise particle migration—is investigated. For each of these studies, a thorough literature review will outline past findings and motivate the further study of the systems in question.

1.0.3 Suspension rheology

Expanding upon the initial work of Einstein discussed in Section 1.0.1, several investigators have examined the non-Newtonian rheology of suspensions. Non-Newtonian effects can occur due to a polymeric solvent or high particle concentration. Past work for each of these cases will be reviewed below, along with the combined case of a polymeric, highly concentrated particle suspension.

The use of a polymeric solvent yields non-Newtonian effects in both dilute and concentrated suspensions. In the dilute particle limit, the bulk properties of the suspension are given by the sum of the solution properties plus a term that is linear in particle concentration. Hence, the suspension displays the non-Newtonian behavior of the solution alone plus additional contributions arising from

the polymer-particle interactions. Several theoretical studies have addressed this problem using a second-order fluid model, which gives qualitative predictions for the slow deformation limit (where De is small), as discussed in Section 1.0.2. In a recent study, Koch & Subramanian [17] found enhancement of both the first and second normal stress differences due to the presence of particles. Numerical work by Patankar & Hu [19] demonstrated a linear scaling with De of the first normal stress difference up to $De = 0.2$. These Finite Element Method simulation results qualitatively agree with the second-order fluid studies at low De. However, they are limited to two dimensional effects and thus do not examine the second normal stress difference. They also examine a small range of De, leaving the question of the effect of finite polymer relaxation time on suspension rheology unanswered. Experimental work in the area of suspension rheology is a bit more extensive, but most of the experiments study systems that do not conform to the restrictions of the theoretical and numerical work and cannot easily be compared. It also should be noted that one or more microstructural effects can occur in an experiment that alter suspension rheology, depending on the set-up. These include particle-particle and particle-wall interactions, as well as cross-streamline particle migration, which is thoroughly introduced in the following section. The result of these effects is a complex, inhomogeneous particle distribution. While experimental studies are useful for studying suspension properties and their effects on processing properties, the isolation of the effect of polymer-particle interactions at the particle length scale is limited by the complexity introduced by the other microstructural effects. Highgate & Whorlow [11] tried to avoid some of the problems mentioned above by taking measurements at very short times and found that the addition of particles shifted the viscosity and normal stress differences by an amount independent of shear stress. They found that the viscosity increased by a greater amount than the first normal stress difference, which led to a decrease in the fluid elasticity.

Newtonian suspensions can also display non-Newtonian behavior, with normal stress differences developing in concentrated particle systems due to asymmetrical microstructure caused by particle-particle flow field interactions [23]. No other non-Newtonian effects such as shear thinning/thickening occur in these suspensions. The irreversible interactions can occur due to the surface roughness [23] or Brownian motion [10] of the particles. Experiments [28] and simulations [26],[10] show that particle suspensions in Newtonian flows give negative first normal stress differences for most cases. Foss & Brady [10] found that the sign of the first normal stress difference depends on the Péclet (Pe) number, defined as $Pe = \frac{LV}{D}$, where L is the characteristic length, V is the characteristic velocity, and D is the diffusion coefficient. High Pe (where hydrodynamic interactions dominate) gives a negative first normal stress coefficient and low Pe (where Brownian interactions dominate) gives a positive first normal stress coefficient. Zarraga [28] and Foss & Brady [10] found negative second normal stress differences for all Pe, with $|N_2|$ being significantly greater than $|N_1|$.

Researchers have also investigated the combined effect of concentrated suspensions in non-Newtonian fluids. Based on the individual contributions to the normal stress difference due to the polymers and to the high particle concentration, the second normal stress difference should be negative, while the first normal stress difference could be positive or negative due to the competition between the two terms. All of the experimental data for non-Newtonian suspensions has shown a positive first normal stress difference, although it is likely that with the proper choice of polymer and concentration of particles, one could observe a negative first normal stress difference. Mall-Gleissle et al. [18] plotted the first normal stress difference against the shear stress, showing that the first normal stress difference is positive, but it decreases in magnitude with higher volume fraction at a given shear

stress. They found that the second normal stress difference, in contrast, increases in magnitude with increasing particle concentration. Zarraga et al. [29] found that the properties of the non-Newtonian polymer solution were more important in defining the first normal stress difference than the polymer-particle interactions, but the polymer solution was irrelevant in the case of the second normal stress difference, which was approximately the same as that found in the Newtonian suspension. They found a linear relationship between the first normal stress difference (normalized by the shear stress) and De in the high volume fraction systems that they studied. In a computational study examining the rheology of of circular particles suspended in an Oldroyd-B fluid, Hwang et al. [15] showed results for the first normal stress difference for a dilute suspension up to $We = 1$, also finding it to be positive and increasing with increasing particle concentration, in contrast to the experimental results. However, their results seem to show clustering effects even in the limit of low particle concentration, as the scaling of the ratio of the first normal stress difference to the shear viscosity with the particle concentration is quadratic in particle concentration for the dilute limit. This is possibly due to the fact that they only used a maximum of six particles in their simulations.

In summary, based on the past literature, one can conclude that the overall bulk stress is governed by the competition between the polymeric fluid-particle interactions and the inhomogeneous microstructure in concentrated systems. These two contributions are in the opposite direction for the first normal stress difference and the same direction (negative) for the second normal stress difference. However, despite some advances in the general understanding of particle concentration on suspension rheology, many questions remain in the field of rheology. This thesis will address one important question, which is the determination of the effects of finite polymer relaxation time on polymer-particle interactions. While some exper-

imental work has examined this effect, the results are difficult to interpret due to the many simultaneous flow field effects that occur. The normal stress differences change based on the particle concentration and the polymeric solution properties; in addition, the shear rate dependent polymer-particle interactions are difficult to measure, as they are masked by the changes in the polymer solution itself. In order to isolate the effect of the polymer-particle interaction, it is necessary to use a polymeric fluid that is entirely elastic and does not have shear rate dependent properties (Boger fluid described by the Oldroyd-B constitutive model), which is what is done in this thesis. Other complicating inhomogeneous microstructural effects due to particle migration or clustering are avoided by studying a dilute suspension without particle-particle and particle-wall hydrodynamic effects. It would be of interest to continue the work of this thesis by performing experiments on highly elastic Boger fluids in a dilute suspension in order to verify the predictions of the quasi-analytical method presented in Chapter 2.

1.0.4 Particle migration

Inertia-induced particle migration was first experimentally observed by Segré and Silberberg [24], [25]. They found that neutrally buoyant, rigid spheres suspended in a Poiseuille flow migrated to an equilibrium point between the center and wall of the channel. Since their discovery, a number of other investigators have studied the curious effect of particle motion perpendicular to the bulk streamlines. Several factors have proved important in characterizing the magnitude and direction of the cross-stream force or velocity of a suspended particle and will be summarized briefly.

In a series of theoretical investigations, Leal & coworkers [13], [12], [8], [7]

performed second order fluid perturbation analyses to further the fundamental understanding of particle migration. Ho & Leal [12] found that in an inertial flow, spherical particles migrated to the center of the channel in a Couette flow, while they migrated to a position of 0.6 times the channel half width from the center line in a Poiseuille flow. In the area of viscoelastic flow, Ho & Leal [13] found that rigid, neutrally buoyant spheres migrate to the center of a Poiseuille flow and to the outer wall of a circular Couette flow, in both cases where the absolute shear rate is at its minimum. Chan & Leal expanded upon the previous analyses, relaxing the condition of a rigid particle by applying a deformable surface boundary condition in order to study drops [8], [7]. While the overall qualitative result of the direction of migration did not change, the equations differed significantly, and thus the predicted migration velocity changed based on complexity of the 3D bulk flow. The perturbation analyses, while useful for describing predominantly elastic flows, do not describe the shear thinning behavior that many polymer solutions exhibit at higher shear rates. Experiments are useful in filling in the gaps for which the theory does not apply. Jefri & Zahed [16] corroborated the previous theoretical findings with experiments of spheres in different types of polymeric fluids. They found spheres suspended in a Boger (highly elastic) fluid migrate toward the center of the channel in 2D Poiseuille flows, as predicted by the theory. However, they found that spheres suspended in fluids with low elasticity and high shear thinning actually migrate toward the wall in a 2D Poiseuille flow.

The overall conclusions that one can draw from these studies are that there are two principal ways in which to induce particle migration—through an appropriate selection of a low viscosity fluid or a large particle size to give rise to inertial effects or through the use of a viscoelastic solvent. Inertial migration can be described as a competition between two terms, one which comes from the interaction of the par-

ticle stresslet with the bulk shear and the other which comes from the interaction of the particle stresslet with the curvature of the bulk velocity field. These two competing forces point in opposite directions, with the first term pointing toward the center of a flow, and the second toward the the direction of increasing shear rate [12]. Particle migration due to a polymeric fluid is governed by inhomogeneous stretch of the suspended polymers, with the larger polymer stresses occurring in areas of larger shear rate, thus causing the particle to migrate to the area with the lowest absolute shear rate.

More recent studies in particle migration added confusion to the fundamental understanding of the phenomenon, finding that elastic fluids sometimes caused particles to migrate in the opposite direction from that which was predicted by the perturbation analyses. Carew & Townshend [6] found that a fixed cylinder experienced a cross-stream force toward the wall in a viscoelastic Poiseuille flow. Dhahir & Walters [9] performed experiments in a Poiseuille flow device in which they measured the cross stream force acting on a large, freely rotating cylinder fixed in the bulk flow direction. They found that for both Boger and pseudo plastic fluids that the cross-stream force pointed toward the wall. Huang, Hu, & Joseph [14] performed a computational particle migration study on inertial, viscoelastic fluids. Examining the limit of low Re, where inertial effects are negligible, they dropped the nonlinear inertial term in the Navier-Stokes equation, but they kept the transient inertial term ($\partial u/\partial t$). They found that the migration direction of a cylinder in an Oldroyd-B Poiseuille flow depends on the particle size, with large particles migrating to the wall and small particles migrating toward the center. The more recent experimental and numerical results raised questions such as what effects the particle boundary condition, the suspending fluid type, and the particle size have on the qualitative results. The fundamental explanations for the impact

of these parameters also remained unresolved, motivating a theoretical study in the area of particle migration to explain the contradictory phenomena occurring.

1.0.5 Motivation and summary of results

From an overall standpoint, research in the field of viscoelastic suspensions seeks to determine macroscopic rheological properties while also characterizing microstructural effects such as particle migration and particle-particle interactions, with the goal of being able to develop overall constitutive models that accurately describe the suspension stress. Some progress has been made in the area of concentrated Newtonian particle suspensions [21], [4], where constitutive models were developed that predict concentration-dependent non-linear behaviors in the suspension viscosity and normal stress differences. However, most of the individual microstructural effects are studied in isolation; in many cases, the current literature does not agree on many fundamental qualitative behaviors on the particle scale. There is significant confusion in the literature over microstructural effects such as the correct direction of particle migration. Further, some essential questions have not been answered such as the behavior of the shear rate dependent rheological properties of η, N_1, and N_2 in a particle suspension with a finite relaxation time. Without a basic understanding of polymer-particle interactions on the particle scale, it is impossible to accurately predict suspension inhomogeneities, and thus suspension properties based on particle, fluid, and flow properties.

Motivated by the applications and fundamental understanding of polymer suspension applications, a further understanding of the fluid behavior at the particle level is necessary in order to accurately predict macroscopic suspension properties. In the rheology study discussed in chapter 2, contributions at O(c) to the suspen-

sion stress include the modification of 1) the polymer stress due to the particle-induced changes in the Newtonian flow field 2) the Newtonian particle stresslet by the polymeric fluid, and 3) the Newtonian flow field due to the polymer, which changes the particle stresslet. The shear viscosity and first normal stress difference are found to shear thicken while the second normal stress difference coefficient is found to thicken at low shear rates and thin at high shear rates.

Due to confusion in the literature over even the direction of particle migration in a viscoelastic suspension, it was appropriate to re-examine the problem from a fundamental theoretical standpoint, resolving the discrepancies between previous theoretical [13], [5], experimental [16], [9], and simulation [14], [6] work. In the particle migration study discussed in chapter 3, it is found that a neutrally buoyant particle migrates toward the center of the channel for all particle sizes and cross-stream positions. In contrast, a cylinder fixed in position is found to experience a cross-stream force directed toward the wall. These findings resolve the contradictory results in the literature, showing that the direction of the cross-stream force depends on the particle boundary condition.

REFERENCES

[1] H. A. Barnes. A review of the rheology of filled viscoelastic systems. *Rheology Reviews*, pages 1–36, 2003.

[2] G. K. Batchelor. The effect of Brownian motion on the bulk stress in a suspension. *J. Fluid Mech.*, 83:97–117, 1977.

[3] J. F. Brady and G. Bossis. The rheology of concentrated suspensions of spheres in simple shear flow by numerical simulation. *J. Fl. Mech.*, 155:105–29, 1985.

[4] J. F. Brady and M. Vicic. Normal stresses in colloidal dispersions. *J. Rheol.*, 39:545–566, 1995.

[5] P. O. Brunn. The motion of rigid particles in viscoelastic fluids. *J. Non-Newt. Fluid Mech.*, 7:271, 1980.

[6] E. O. A. Carew and P. Townsend. Slow visco-elastic flow past a cylinder in a rectangular channel. *Rheol. Acta*, 30:58–64, 1991.

[7] P. C.-H. Chan and L. G. Leal. A note on the motion of a spherical particle in a general quadratic flow of a second-order fluid. *J. Fluid Mech.*, 82:549–559, 1977.

[8] P. C.-H. Chan and L. G. Leal. The motion of a deformable drop in a second-order fluid. *J. Fluid Mech.*, 92:131–170, 1979.

[9] S. A. Dhahir and K. Walters. On non-newtonian flow past a cylinder in a confined flow. *J. Rheol.*, 33:781, 1989.

[10] D. R. Foss and J. F. Brady. Structure, diffusion and rheology of brownian suspensions by stokesian dynamics simulation. *J. Fluid Mech.*, 407:167–200, 2000.

[11] D. Highgate and R. Whorlow. Rheological properties of suspensions of spheres in non-newtonian media. *Rheol. Acta*, 9:569–576, 1970.

[12] B. P. Ho and L. G. Leal. Inertial migration of rigid spheres in two-dimensional unidirectional flows. *J. Fluid Mech.*, 65:365–400, 1974.

[13] B. P. Ho and L. G. Leal. Migration of rigid spheres in two-dimensional unidirectional shear flow of a second order fluid. *J. Fluid Mech.*, 76:783–799, 1976.

[14] P. Huang, J. Feng, H. Hu, and D. Joseph. Direct simulation of the motion of solid particles in Couette and Poisseiulle flows of viscoelastic fluids. *J. Fluid Mech.*, 343:73–94, 1997.

[15] W. R. Hwang, M. A. Hulsen, and H. E. H. Meijer. Direct simulations of particle suspensions in a viscoelastic fluid in sliding bi-periodic frames. *J. Non-Newt. Fl. Mech.*, 121:15–33, 2004.

[16] M. A. Jefri and A. H. Zahed. Elastic and viscous effects on particle migration in plane-poiseuille flow. *J. Rheol.*, 33:691, 1989.

[17] D.L. Koch and G. Subramanian. The stress in a dilute suspension of spheres suspended in a second-order fluid subject to a linear velocity field. *J. Non-Newt. Fluid Mech.*, 138:87–97, 2006.

[18] S. E. Mall-Gleissle, W. Gleissle, G. H. McKinley, and H. Buggisch. The normal stress behaviour of suspensions with viscoelastic matrix fluids. *Rheol Acta*, 41:61–76, 2002.

[19] N. A. Patankar and H. H. Hu. Rheology of a suspension of particles in viscoelastic fluids. *J. Non-Newt. Fl. Mech.*, 96:427–443, 2001.

[20] C. J. S. Petrie. The rheology of fibre suspensions. *J. Non-Newt. Fl. Mech.*, 87(2-3):369–402, 1999.

[21] N. Phan-Thien, X. Fan, and B. C. Khoo. A new constitutive model for monodispersed suspensions of spheres at high concentrations. *Rheol. Acta*, 38:297–304, 1999.

[22] D. Quemada and C. Berli. Energy of interaction in colloids and its implications in rheological modeling. *Advances in Colloid and Interface Science*, pages 51–85, 2002.

[23] I. Rampall, J. R. Smart, and D. T. Leighton. The influence of surface roughness on the particle-pair distribution function of dilute suspensions of non-colloidal spheres in simple shear flow. *J. Fluid Mech.*, 339:1–24, 1997.

[24] G. Segré and A. Siberburg. Behaviour of macroscopic rigid spheres in poiseuille flow part 1. determination of local concentration by statistical analysis of particle passages through crossed light beams. *J. Fluid Mech.*, 10:571, 1962.

[25] G. Segré and A. Silberberg. Non-newtonian behavior of dilute suspensions of macroscopic spheres in a capillary viscometer. *J. Colloid Sci.*, 18:312, 1963.

[26] A. Singh and P. R. Nott. Normal stresses and microstructure in bounded sheared suspensions via stokesian dynamics simulations. *J. Fluid Mech.*, 412:279–301, 2000.

[27] R. I. Tanner. *Engineering Rheology*. Oxford Univ. Press, 1992.

[28] I. E. Zarraga, D. A. Hill, and D. T. Leighton. The characterization of the total stress of concentrated suspensions of noncolloidal spheres in newtonian fluids. *J. Rheol.*, 44(2):185–220, 2000.

[29] I. E. Zarraga, D. A. Hill, and D. T. Leighton. The characterization of the total stress of concentrated suspensions of noncolloidal spheres in newtonian fluids. *J. Rheology*, 44:185–220, 2000.

Chapter 2

The stress in a dilute suspension of spheres in a dilute polymer solution at finite Deborah numbers subject to simple shear flow

2.1 Summary

The ensemble average stress in a dilute suspension of spheres is determined for the low polymer concentration limit. Contributions to the non-Newtonian bulk stress arise from the interaction of particles and polymers in the suspension. The coupled effects give rise to a contribution to the particle stresslet due to the presence of the polymer and an extra polymer stress due to the alteration of the flow field by the particles. Employing an Oldroyd-B constitutive equation, this study predicts behavior at high Deborah number (De), defined as the fluid relaxation time divided by the characteristic flow time. At finite De, the viscosity and first normal stress difference coefficient display shear thickening behavior while the second normal stress difference coefficient shows positive deviations for low De but switches sign at approximately $De = 4$.

2.2 Introduction

The rheology of non-Newtonian particle suspensions is of practical significance in a variety of industrial applications, including tissue engineering [8], injection molding [15], cosmetics [13], and food science [3]. The complex behaviors of vis-

coelastic suspensions give rise to challenges in material processing, affecting fluid properties such as die swell and the onset of flow instabilities. These challenges have motivated numerous studies that examine the stress fields and the resultant rheological properties of polymeric suspensions. However, previous work in the development of the theory for suspension rheology has been confined to low Deborah number (De) and thus has not shown the effect of finite relaxation time on suspension rheology. Previous numerical studies, although performed at a higher range of De, have been confined to 2D flows and thus do not provide a complete understanding of real systems with 3D rheological effects. Thus, to date, there is an incomplete understanding of the effects of finite polymer relaxation time on the flow and stress fields and the associated changes in the rheological properties of dilute non-Newtonian particle suspensions.

Many authors have modeled the rheology of dilute suspensions with a second-order fluid stress equation, which has the advantage of being analytically tractable due to its relative mathematical simplicity. Recently, Koch & Subramanian [10] found expressions for the particle contributions to the first and second normal stress difference coefficients (ψ_1^P and ψ_2^P, respectively) in a perturbation expansion about small De. They found that the particle contributions are related to the suspending fluid normal stress difference coefficients (ψ_1^0 and ψ_2^0) and the particle volume fraction (ϕ), with the final expressions given as $\psi_1^P = \frac{5}{2}\phi\psi_1^0$ and $\psi_2^P = \frac{75}{28}\phi\psi_2^0 + \frac{5}{56}\phi\psi_1^0$. As can be seen, they predicted enhancement of both of the normal stress differences due to the presence of particles. They found that the O(De) particle contributions to the ensemble average suspension stress arise from 1) the polymer stress field altered by the particle-induced velocity disturbance, 2) the polymeric fluid altering the particle stresslet, and 3) the changes in the Newtonian velocity and pressure fields caused by the polymeric fluid, which alter the particle

stresslet.

Several earlier investigators (Kaloni & Stasna [9], Sun & Jayaraman [16], and Mifflin [12]) attempted to determine the expression for all or part of the second-order fluid suspension stress; however, Koch & Subramanian [10] found that each of these authors made conceptual errors or omitted certain terms in the calculation of the bulk stress. In a recent study, Greco et al. [4] found the same expression for the particle stresslet as Koch & Subramanian [10] but argued that the average polymer stress should be zero. This argument did not make sense, given the fact that the average of the deviation of the rate of strain tensor from its mean value dotted with itself (a contribution arising from the second-order fluid constitutive equation) is the average of a positive definite quantity.

All of the theoretical studies, by virtue of the choice of constitutive equation, are limited by the requirement of low De in order to satisfy the conditions necessary for a second-order fluid, and thus the results do not apply to non-Newtonian suspensions where the polymer relaxation time is high or the fluid relaxation time is low. The present study is important in expanding the theory of non-Newtonian suspensions to predict high De conditions. We use the Oldroyd-B constitutive model, which in addition to being valid for finite De, has the advantage of describing a polymeric fluid with a viscosity and a first and second normal stress difference that are independent of shear rate. This property makes it possible to isolate the particle-polymer interactions by removing any shear rate dependent effects arising from the fluid itself.

The experimental work to date unfortunately has not used fluids that decouple the particle-polymer interactions from the shear rate dependent nature of the base fluid, which prevents the direct comparison of results between experiment and

the present study. Experiments with Boger fluids (which are accurately described by the Oldroyd-B constitutive equation) would enhance the understanding of the shear rate dependent effects on the particle-polymer interactions, without having the common problem of the shear rate-dependent particle-polymer interactions being masked by the shear rate-dependent polymeric solvent effects. Nevertheless, past experimental studies, along with some 2D numerical work, provide qualitative information useful in understanding suspension rheology.

In the dilute limit, Highgate & Whorlow [6] did some of the first experimental work in determining the rheological properties of viscoelastic suspensions. They attempted to avoid the common experimental problems of particle migration and clustering by performing experiments on short time scales. For a range of different viscoelastic solutions, they found that the addition of particles to a viscoelastic fluid yielded an increase in both the viscosity and normal stress differences that was independent of shear stress of the base fluid for a given particle concentration. They found that the addition of particles increased the viscosity and the first normal stress difference by appoximately the same percentage in the dilute particle limit. In a numerical study, Patankar & Hu [14] performed finite element simulations using the Oldroyd-B constitutive equation, finding that the first normal stress difference in a dilute suspension increases linearly up to $De = 0.18$. They noted that the addition of a particle enhanced the first normal stress difference and that this enhancement increased with the elasticity of the fluid. These results agree with the qualitative predictions of the second-order fluid investigations but do not extend to a De high enough to see finite polymer relaxation time effects.

In the realm of more concentrated suspensions, Hwang et al. [7] performed a 2D Oldroyd-B computational study that examined particle concentration effects on suspension rheology. They looked at systems consisting of one, two, and six

particles, with Weissenburg numbers ranging from zero to 2.5. For dilute systems, they presented results up to $De = 1$, finding that their results matched the second-order fluid limit predictions. For systems at higher concentration, they found that the suspension exhibited shear-thickening behavior for both the shear viscosity and the first normal stress difference. Systems at higher De displayed greater shear thickening than low De simulations at the same concentration. However, their results seem to show clustering effects even in the limit of low particle concentration, as the scaling of the ratio of the first normal stress difference to the shear viscosity with the particle concentration is quadratic in particle concentration for the dilute limit. In an experimental study, Zarraga et al. [18] did measurements on high concentrations ($\geq$30%) of particles suspended in a viscoelastic fluid, finding that ψ_1 was positive and ψ_2 was negative. These results are in contrast to Newtonian results Zarraga et al. [17] which have a positive first normal stress difference, thus indicating that viscoelasticity is more important than particle concentration in determining qualitative trends. Zarraga et al. [18] concluded that the second normal stress difference was largely independent of the viscoelastic fluid, with their results approximating Newtonian results at high particle concentration. While the signs of the normal stress differences match the second-order fluid results of Koch & Subramanian [10], the quantitative results do not match nearly as well. This can be attributed to several possible factors. At sufficiently high particle volume fraction, particle aggregation or chaining occurs [11], leading to inhomogeneous systems with different rheological properties. Particle-wall hydrodynamic interactions can also be significant. Additional interactions between the particles and the polymer phase can occur as well, with polymers absorbing on the particle surface, effectively increasing the particle size [1].

In light of the past work, we examine the effects of finite polymer relaxation

time on particle-polymer interactions in a dilute suspension in the low polymer concentration limit, seeking to understand the associated non-linear behaviors of the viscosity and normal stress differences. The Oldroyd-B fluid, which is ideally suited for studying the low concentration limit, is employed in order to determine the suspension stress through the computational integration of the quasi-analytical formulation of the particle stresslet and average polymer stress differential equations. Our small polymer concentration perturbation analysis has many similarities to the small De perturbation analysis of Koch & Subramanian [10], which will be highlighted in the formulation of the stress. These include the use of an ensemble average approach in order to formulate a well posed integral of the polymer stress and the use of the reciprocal theorem to avoid solving explicitly for the non-Newtonian perturbation to the Newtonian velocity and pressure fields, which contribute to the particle stresslet. The first section will outline the governing equations and will show the contributions to the bulk suspension stress due to polymer-particle interactions. The next section will delineate the details of the perturbation analysis about concentration for the particle suspension and describe the computational method. The last section will present the results of the computation, confirming the stress contributions in the low De limit with previous theoretical work and then expanding these results up to a Deborah number of 19.

2.3 Stress formulation

We first consider the stress in the pure fluid phase without any particles. Since the fluid viscosity is high in most viscoelastic fluid applications, the Reynolds number is negligibly small, and we neglect inertial terms in the Cauchy momentum equation. The equations describing a general Stokes flow are the continuity and momentum

equations, written as follows—

$$\nabla \cdot \boldsymbol{u} = 0, \tag{2.1}$$

$$\nabla \cdot \boldsymbol{\sigma} = 0, \tag{2.2}$$

where $\boldsymbol{u}$ is the velocity field and $\boldsymbol{\sigma}$ is the overall stress tensor.

The flow field is specified to be a simple shear flow—

$$\tilde{\boldsymbol{u}} = \boldsymbol{e}_1 r_2, \tag{2.3}$$

where the tilde indicates a pure fluid quantity without the presence of particles. The coordinate system is defined such that coordinate 1 is the direction of the flow, 2 is the direction of the velocity gradient, and 3 is the direction of the vorticity. The quantities above are non-dimensionalized with the characteristic length scale a and the characteristic velocity scale $a\dot{\gamma}$, where a is the particle radius and $\dot{\gamma}$ is the shear rate.

The stress is written as

$$\tilde{\boldsymbol{\sigma}} = -\tilde{p}\boldsymbol{\delta} + 2\tilde{\boldsymbol{e}} + \tilde{\boldsymbol{\Pi}}, \tag{2.4}$$

where $\tilde{\boldsymbol{\Pi}}$ is the polymer stress tensor and the rate of strain tensor $\tilde{\boldsymbol{e}}$ is defined as

$$\tilde{\boldsymbol{e}} = \frac{1}{2}(\nabla\tilde{\boldsymbol{u}} + \nabla\tilde{\boldsymbol{u}}^T). \tag{2.5}$$

The stress is non-dimensionalized by $\eta_s\dot{\gamma}$, where η_s is the solvent viscosity. All quantities that follow will be non-dimensionalized using the same scales as defined above, unless otherwise noted.

The polymer stress $\tilde{\boldsymbol{\Pi}}$ is defined as $\frac{c\boldsymbol{A}}{De}$, where c is the polymer concentration and $\boldsymbol{A}$ is the polymer conformation tensor, defined as $\langle \boldsymbol{qq} \rangle$, where $\boldsymbol{q}$ is the connector vector defining the end to end position vector for the polymer. The Oldroyd-B

constitutive equation gives the polymer stress and is defined in terms of $\boldsymbol{A}$ as follows—

$$\frac{DA_{ij}}{Dt} = A_{kj}\frac{\partial u_i}{\partial r_k} + A_{ik}\frac{\partial u_j}{\partial r_k} - \frac{1}{De}(A_{ij} - \delta_{ij}), \tag{2.6}$$

where $\boldsymbol{A}$ is equal to $\langle \boldsymbol{qq} \rangle$ and $\boldsymbol{q}$ is defined as the bead separation position vector for the polymer dumbbell model, normalized by the radius of gyration of the polymer. The Oldroyd-B equation is developed from kinetic theory, with polymer molecules considered as two beads connected by a Hookean spring. The Deborah number De is thus defined as $\lambda_H \dot{\gamma}$, where λ_H is the relaxation time for the Hookean spring.

In order to determine the suspension stress from the constitutive equation (Equation 2.6), we write Equation 2.4 in terms of the polymer conformation tensor—

$$\tilde{\boldsymbol{\sigma}} = -\tilde{p}\boldsymbol{\delta} + 2\tilde{\boldsymbol{e}} + \frac{c\tilde{\boldsymbol{A}}}{De}. \tag{2.7}$$

We next need a similar equation for the combined particle and fluid system in order to determine the bulk stress of the suspension. In order to do this, we consider a system in which the microscopic particle scale is much smaller than the macroscopic system length scale; with this condition, the suspension can be seen as a homogenous fluid with unique rheological properties that can be determined through an averaging technique. Batchelor [2] derived the general expression for the stress in a particle suspension, which is reproduced here, with the additional polymer stress included—

$$\langle \boldsymbol{\sigma} \rangle = -p_{susp}\boldsymbol{\delta} + 2\langle \boldsymbol{e} \rangle + \frac{c\langle \boldsymbol{A} \rangle}{De} + n\int_{|\boldsymbol{r}-\boldsymbol{r}_1|\leq 1} d\boldsymbol{r}_1 \langle \boldsymbol{\sigma^E} \rangle_1(\boldsymbol{r}|\boldsymbol{r}_1), \tag{2.8}$$

where n is the number of particles per volume. The brackets indicate an ensemble averaged quantity and $\langle \boldsymbol{\sigma^E} \rangle_1(\boldsymbol{x}|\boldsymbol{r}_1)$ is the conditional ensemble average of the extra stress at a position $\boldsymbol{r}$ over configurations in which a particle is centered at $\boldsymbol{r_1}$. An ensemble includes all possible configurations of particles and these are averaged in

order to find mean values of pertinent quantities (in this case, the extra polymer stress and particle stresslet), with the ensemble average of a quantity A formally defined as

$$\langle A \rangle = \int d\boldsymbol{r_1} \dots d\boldsymbol{r_N} P(\boldsymbol{r_1}, \dots \boldsymbol{r_N}) A \tag{2.9}$$

where P is a probability function. See Batchelor [2] for a complete theory on ensemble averaging. The last term in Equation 2.8 ($\boldsymbol{\sigma^E}$) is defined as the extra stress term, which includes the additional stress in the particle phase and the additional stress that would occur if the fluid stress equation applied inside the particle [2]. The stress in the particle phase is not equal to the stress in the fluid phase at the particle boundary because of the zero rate of strain in the particle phase, and thus there is a step change in the stress at the particle boundary. However, this step change in rate of strain at the particle surface only gives a contribution to the isotropic part of the average stress [10]. Since we are only interested in determining the normal stress differences and the viscosity, we will only consider the deviatoric part of the dimensional stress; then, Equation 2.8 becomes

$$\langle \hat{\boldsymbol{\sigma}} \rangle = 2\langle \hat{\boldsymbol{e}} \rangle + \frac{c}{De} \langle \hat{\boldsymbol{A}} \rangle + n\hat{\boldsymbol{S}}. \tag{2.10}$$

Here, the stresslet $\hat{\boldsymbol{S}}$ is defined as

$$\hat{\boldsymbol{S}} = \int_{|\boldsymbol{r}_1 - \boldsymbol{r}| \leq 1} d\boldsymbol{r}_1 \langle \hat{\boldsymbol{\sigma}} \rangle_1 (\boldsymbol{r} | \boldsymbol{r}_1), \tag{2.11}$$

where the hats in the preceding two equations denote the deviatoric part of a quantity. Applying the divergence theorem, the stresslet can be written as a surface integral as follows—

$$\hat{\boldsymbol{S}} = \int_{|\boldsymbol{r}_1 - \boldsymbol{r}| \leq 1} dA \mathrm{sym}[\boldsymbol{nn} \cdot \langle \hat{\boldsymbol{\sigma}} \rangle_1 (\boldsymbol{r} | \boldsymbol{r}_1), \tag{2.12}$$

Using the conditions that 1) the particle volume fraction is small enough that particle-particle interactions are negligible and 2) the fluid velocity approaches the

ensemble average velocity far from the particle, the particles in the suspension can be treated as isolated spheres [2]. Then, the average ensemble stress is related to the product of the stress around a single particle and the particle volume fraction ϕ. Using these conditions and applying the divergence theorem, the stresslet in Equation 2.11 can then be expressed in a simpler form—

$$\hat{\boldsymbol{S}} = \int_{r=1} dA \text{sym}[\boldsymbol{nn} \cdot \hat{\boldsymbol{\sigma}}]. \tag{2.13}$$

For the equations that follow, in order to simplify the presentation, the non-bracketed quantities will denote the case of an isolated particle, with the coordinate system centered at the particle center.

Having defined the stresslet, we can now begin to calculate the individual terms in Equation 2.10. In order to do this, we will expand about small polymer concentration, keeping the leading order and first order terms—

$$\langle \hat{\boldsymbol{\tau}} \rangle = \langle \hat{\boldsymbol{\tau}}_{\boldsymbol{0}} \rangle \tag{2.14}$$

$$c\langle \hat{\boldsymbol{A}} \rangle = c\langle \hat{\boldsymbol{A}}_{\boldsymbol{0}} \rangle + O(c^2) \tag{2.15}$$

$$\hat{\boldsymbol{S}} = \hat{\boldsymbol{S}}_{\boldsymbol{0}} + c\hat{\boldsymbol{S}}_{\boldsymbol{1}} + O(c^2). \tag{2.16}$$

From the above equations, it is clear that we need to calculate four terms— $\langle \hat{\boldsymbol{\tau}}_{\boldsymbol{0}} \rangle$, $\langle c\hat{\boldsymbol{A}}_{\boldsymbol{0}} \rangle$, $\langle \hat{\boldsymbol{S}}_{\boldsymbol{0}} \rangle$, and $\langle c\hat{\boldsymbol{S}}_{\boldsymbol{1}} \rangle$. It should be noted that $c\langle \hat{\boldsymbol{\tau}}_{\boldsymbol{1}} \rangle$ is zero, as the average rate of strain is specified as $\langle \boldsymbol{e}_0 \rangle$, and thus higher order rate of strain terms are zero. We will consider each of the contributing terms in turn, starting with the Newtonian stress. To calculate the leading order velocity and pressure fields, a multipole expansion of Equation 2.2 for a particle of radius r centered at $r = 0$ is performed, giving—

$$u_{i,0} = \tilde{e}_{ji} r_j + \tilde{\omega}_{ji} r_j + \frac{5}{2}\left(\frac{1}{r^7} - \frac{1}{r^5}\right) \tilde{e}_{jk} r_j r_k r_i - \frac{1}{r^5} \tilde{e}_{ji} r_j, \text{ for } r \geq 1, \tag{2.17}$$

$$u_{i,0} = \tilde{\omega}_{ji} r_j, \text{ for } r < 1, \tag{2.18}$$

and

$$p_0 = -\frac{5}{r^5}\tilde{e}_{jk}r_j r_k, \text{ for } r \geq 1, \tag{2.19}$$

where

$$\tilde{\boldsymbol{\omega}} = \frac{1}{2}(\nabla\tilde{\boldsymbol{u}} - \nabla\tilde{\boldsymbol{u}}^T). \tag{2.20}$$

The leading order stress tensor is then

$$\begin{aligned}\hat{\tau}_{il,0} =&(\tilde{e}_{il} + \tilde{e}_{li}) + 5\left(\frac{1}{r^7} - \frac{1}{r^5}\right)\left(\tilde{e}_{lk}r_k r_i + \tilde{e}_{jl}r_j r_i + 2\tilde{e}_{jk}r_j r_k\delta_{il}\right.\\ &\left. + \tilde{e}_{ik}r_k r_l + \tilde{e}_{ji}r_j r_l\right) - \left(\frac{35}{r^9} + \frac{25}{r^5}\right)\tilde{e}_{jk}r_i r_j r_k r_l - \frac{1}{r^5}\left(\tilde{e}_{li} + \tilde{e}_{il}\right)\\ &+ \frac{5r_j}{r^7}\left(\tilde{e}_{ji}r_l + \tilde{e}_{jl}r_i + \frac{5}{r^5}\tilde{e}_{jk}r_j r_k\delta_{il}\right).\end{aligned} \tag{2.21}$$

2.3.1 Average Polymer Stress

Having calculated the Newtonian stress, we next find the average polymer stress $\langle\hat{\boldsymbol{\Pi}}_{\mathbf{0}}\rangle$. Due to the slowly decaying terms associated with the polymer stress, the calculation of $\langle\hat{\boldsymbol{\Pi}}_{\mathbf{0}}\rangle$ and hence $\langle\hat{\boldsymbol{A}}_{\mathbf{0}}\rangle$ over an infinite domain is not a well posed problem. Considering the second-order fluid constitutive equation (see Koch & Subramanian [10]), $\langle\hat{\boldsymbol{A}}_{\mathbf{0}}\rangle$ must include $\boldsymbol{e}\cdot\boldsymbol{e}$ terms that go like $1/r^3$ and only converge if the integration volume is spherical. The integrals must converge for an arbitrary volume for the problem to be well posed. In order to find the average polymer stress then, we circumvent the calculation of the non-convergent terms by defining a new tensor $\boldsymbol{A}'_{\mathbf{0}}$:

$$\boldsymbol{A}'_{\mathbf{0}} = \boldsymbol{A}_{\mathbf{0}} - \tilde{\boldsymbol{A}}_{\mathbf{0}} - \boldsymbol{A}^{\boldsymbol{L}}_{\mathbf{0}}, \tag{2.22}$$

where $\tilde{\boldsymbol{A}}_{\mathbf{0}}$ is the conformation tensor for the simple shear flow and $\boldsymbol{A}^{\boldsymbol{L}}_{\mathbf{0}}$ is the conformation tensor that includes all terms that are linear with respect to the particle disturbance velocity $\boldsymbol{u}'$ (that is, terms that do not converge).

The fluid velocity can be written as a sum of the undisturbed simple shear flow ($\tilde{\boldsymbol{u}}$) and the particle velocity disturbance ($\boldsymbol{u'}$):

$$\boldsymbol{u} = \tilde{\boldsymbol{u}} + \boldsymbol{u'}. \tag{2.23}$$

In order to find $\tilde{\boldsymbol{A}}_{\boldsymbol{0}}$, we include only the terms in the Oldroyd-B consitutive equation (Equation 2.6) that are independent of $\boldsymbol{u'}$:

$$\frac{1}{De}\tilde{\boldsymbol{A}}_{\boldsymbol{0}} = \nabla\tilde{\boldsymbol{u}}^{\boldsymbol{T}} \cdot \tilde{\boldsymbol{A}}_{\boldsymbol{0}} + \tilde{\boldsymbol{A}}_{\boldsymbol{0}} \cdot \nabla\tilde{\boldsymbol{u}}. \tag{2.24}$$

The above equation can be solved analytically, and the components of the leading order of $\tilde{\boldsymbol{A}}_{\boldsymbol{0}}$ are as follows— $\tilde{A}_{11} = 1 + 2De^2$, $\tilde{A}_{12} = De$,$\tilde{A}_{22} = \tilde{A}_{33} = 1$, $\tilde{A}_{13} = \tilde{A}_{23} = 0$.

In order to find $\boldsymbol{A}_{\boldsymbol{0}}^{\boldsymbol{L}}$, we write all of the terms that are linear in the disturbance velocity take the most slowly decaying $\boldsymbol{A}$ terms that are proportional to $1/r^3$:

$$\tilde{\boldsymbol{u}} \cdot \nabla\boldsymbol{A}_{\boldsymbol{0}}^{\boldsymbol{L}} - \nabla\tilde{\boldsymbol{u}}^{\boldsymbol{T}} \cdot \boldsymbol{A}_{\boldsymbol{0}}^{\boldsymbol{L}} - \boldsymbol{A}_{\boldsymbol{0}}^{\boldsymbol{L}} \cdot \nabla\tilde{\boldsymbol{u}} + \frac{1}{De}\boldsymbol{A}_{\boldsymbol{0}}^{\boldsymbol{L}} = \nabla\boldsymbol{u'}^{\boldsymbol{T}} \cdot \tilde{\boldsymbol{A}}_{\boldsymbol{0}} + \tilde{\boldsymbol{A}}_{\boldsymbol{0}} \cdot \nabla\boldsymbol{u'}. \tag{2.25}$$

We take the ensemble average, noting that $\langle\boldsymbol{\nabla u}\rangle = \nabla\tilde{\boldsymbol{u}}$ by definition, and thus the right hand side is zero:

$$\tilde{\boldsymbol{u}} \cdot \nabla\langle\boldsymbol{A}_{\boldsymbol{0}}^{\boldsymbol{L}}\rangle - \nabla\tilde{\boldsymbol{u}}^{\boldsymbol{T}} \cdot \langle\boldsymbol{A}_{\boldsymbol{0}}^{\boldsymbol{L}}\rangle - \langle\boldsymbol{A}_{\boldsymbol{0}}^{\boldsymbol{L}}\rangle \cdot \nabla\tilde{\boldsymbol{u}} + \frac{1}{De}\langle\boldsymbol{A}_{\boldsymbol{0}}^{\boldsymbol{L}}\rangle = 0. \tag{2.26}$$

Without the disturbance velocity terms, the linear conformation term $\langle\hat{\boldsymbol{A}}_{\boldsymbol{0}}^{\boldsymbol{L}}\rangle$ is also equal to zero. Thus, our final equation for the deviatoric part of the polymer conformation tensor is

$$\langle\hat{\boldsymbol{A}}_{\boldsymbol{0}}\rangle = \hat{\tilde{\boldsymbol{A}}}_{\boldsymbol{0}} + n\int dV\,\hat{\boldsymbol{A}}_{\boldsymbol{0}}'. \tag{2.27}$$

The above integral is convergent for an arbitrary volume since the non-convergent terms ($\hat{\boldsymbol{A}}_{\boldsymbol{0}}^{\boldsymbol{L}}$) are removed with subtraction in Equation 2.22. At finite De, far from the particle, we can perform a perturbation about the disturbance rate of strain

$\boldsymbol{e'}$ which is much smaller than $\tilde{\boldsymbol{e}}$. Then, $\hat{\boldsymbol{A}}^{\boldsymbol{L}}$ is linear in $\boldsymbol{e'}$ and $\hat{\boldsymbol{A}}'$ is quadratic in $\boldsymbol{e'}$. Even though the differential equations for $\hat{\boldsymbol{A}}'$ and $\hat{\boldsymbol{A}}^{\boldsymbol{L}}$ must be solved at finite De, the dominant contribution determining the solution of these equations comes from the behavior at a distance of order r when computing $\hat{\boldsymbol{A}}(r)$ as long as De is order one. It should also be noted that this integral requires the inclusion of points inside the sphere, which give a contribution to the second term in Equation 2.10. Inside the particle, the only non-zero term is $\hat{\boldsymbol{A}}_{\boldsymbol{0}}^{\boldsymbol{L}}$.

2.3.2 Stresslet

Lastly, the two stresslet terms from Equation 2.10 are determined. The Newtonian term was calculated by Einstein, who found that for a dilute Newtonian suspension of spheres, the particle stresslet is given by

$$\langle \hat{\boldsymbol{S}}_{\boldsymbol{0}} \rangle = \frac{20}{3}\pi \langle \hat{\tilde{\boldsymbol{e}}} \rangle, \tag{2.28}$$

The calculation of the first order contribution $c\langle \hat{\boldsymbol{S}}_{\boldsymbol{1}} \rangle$ requires more effort on our part. This $O(c)$ contribution to the particle stresslet arises from two polymer-particle interactions: one due to the polymer stress that arises from the leading order disturbance velocity field and the other due to the Newtonian stress arising from the $O(c)$ perturbation to the velocity field. We will first consider the contribution due to the Newtonian disturbance velocity field acting on the polymers. This contribution is easily calculated by performing the integral of Equation 2.13 over the surface of the particle —

$$\hat{\boldsymbol{S}}_{\boldsymbol{1}}^{\boldsymbol{A}} = \frac{1}{De}\int \frac{1}{2}[(\boldsymbol{n}\cdot\hat{\boldsymbol{A}}_{\boldsymbol{0}})\boldsymbol{r} + \boldsymbol{r}(\boldsymbol{n}\cdot\hat{\boldsymbol{A}}_{\boldsymbol{0}})]dA. \tag{2.29}$$

Next, the contribution to the stresslet based on the change in the Newtonian stress due to the polymer is defined as follows—

$$\hat{\boldsymbol{S}}_{\mathbf{1}}^{\boldsymbol{B}} = \int \frac{1}{2}[(\boldsymbol{n}\cdot\hat{\boldsymbol{\tau}}_{\mathbf{1}})\boldsymbol{r} + \boldsymbol{r}(\boldsymbol{n}\cdot\hat{\boldsymbol{\tau}}_{\mathbf{1}})]dV. \tag{2.30}$$

This equation cannot be easily integrated, however, because of the difficulty in determining $\hat{\boldsymbol{\tau}}_{\mathbf{1}}$. Instead, a comparison problem is defined, and the solution is found with the reciprocal theorem. This allows $\hat{\boldsymbol{S}}_{\mathbf{1}}^{\boldsymbol{B}}$ to be expressed in terms of the leading order rather than first order velocity field.

Considering the first order stress equation, such that

$$\nabla\cdot\hat{\boldsymbol{\tau}}_{\mathbf{1}} = -\nabla\cdot\hat{\boldsymbol{\Pi}}_{\mathbf{0}}, \tag{2.31}$$

$$\nabla\cdot\boldsymbol{u}_{\mathbf{1}} = 0,$$

$$\boldsymbol{u}_{\mathbf{1}} = 0, \quad \text{at} \quad r = 1,$$

$$\boldsymbol{u}_{\mathbf{1}} \to 0 \quad \text{as} \quad r \to \infty,$$

the comparison problem is a Stokes flow, with

$$\nabla\cdot\hat{\boldsymbol{\Sigma}} = 0, \tag{2.32}$$

$$\nabla\cdot\boldsymbol{v} = 0,$$

$$\boldsymbol{v} = \boldsymbol{B}\cdot\boldsymbol{r}, \quad \text{at} \quad r = 1,$$

$$\boldsymbol{v} \to 0 \quad \text{as} \quad r \to \infty.$$

Dotting Equation 2.31 with $\boldsymbol{u}$ and Equation 2.32 with $\boldsymbol{v}_{\mathbf{1}}$ and then integrating over the fluid volume gives—

$$\int_{V_f} (\nabla\cdot\hat{\boldsymbol{\tau}}_{\mathbf{1}})\cdot\boldsymbol{v} - (\nabla\cdot\hat{\boldsymbol{\Sigma}})\cdot\boldsymbol{u}_{\mathbf{1}}dV = -\int_{V_f} \nabla\cdot\hat{\boldsymbol{\Pi}}_{\mathbf{0}}\cdot\boldsymbol{v}dV. \tag{2.33}$$

Rearranging, we find

$$\int_{V_f} \nabla\cdot(\hat{\boldsymbol{\tau}}_{\mathbf{1}}\cdot\boldsymbol{v} - \hat{\boldsymbol{\Sigma}}\cdot\boldsymbol{u}_{\mathbf{1}})dV = -\int_{V_f} (\nabla\cdot\hat{\boldsymbol{\Pi}}_{\mathbf{0}})\cdot\boldsymbol{u}_{\mathbf{1}}dV.$$

Now we use the divergence theorem and apply boundary conditions to obtain

$$\int_{r\to\infty} \boldsymbol{n}\cdot(\hat{\boldsymbol{\tau}}_{\mathbf{1}}\cdot\boldsymbol{v}-\hat{\boldsymbol{\Sigma}}\cdot\boldsymbol{u}_{\mathbf{1}})dA-\int_{r=1}\boldsymbol{n}\cdot(\hat{\boldsymbol{\tau}}_{\mathbf{1}}\cdot\boldsymbol{B}\cdot\boldsymbol{r})dA=-\int_{V_f}(\nabla\cdot\hat{\boldsymbol{\Pi}}_{\mathbf{0}})\cdot\boldsymbol{v}_{\mathbf{1}}dV, \quad (2.34)$$

where $\boldsymbol{n}$ is the unit outward normal vector. The first integral is negligible, as $\boldsymbol{u_1}$ and $\boldsymbol{v}$ go to zero as $r\to\infty$, and the stresses do not grow with r. The second integral is the ij component of the stresslet, using a definition of $\boldsymbol{B}$ as follows—

$$B_{ijkl}=\frac{1}{2}(\delta_{ki}\delta_{lj}+\delta_{li}\delta_{kj}-\frac{2}{3}\delta_{kl}\delta_{ij}). \quad (2.35)$$

The overall equation for $\hat{\boldsymbol{S}}_{\mathbf{1}}^{\boldsymbol{B}}$ is

$$\hat{\boldsymbol{S}}_{\mathbf{1}}^{\boldsymbol{B}}=\int(\nabla\cdot\hat{\boldsymbol{\Pi}}_{\mathbf{0}})\cdot\boldsymbol{v}_{\mathbf{1}}dV,$$
$$\text{with}\quad \boldsymbol{v}_{\mathbf{1}}=\boldsymbol{B}\cdot\boldsymbol{r},\quad \text{at}\quad r=1. \quad (2.36)$$

The solution to the comparison velocity field is found to be—

$$v_{jkl}=\left(\frac{5}{2r^5}-\frac{5}{2r^7}\right)r_jr_kr_l+\frac{1}{2r^5}(r_k\delta_{jl}+r_l\delta_{jk})+\left(\frac{1}{2r^5}-\frac{5}{6r^3}\right)r_j\delta_{kl}. \quad (2.37)$$

In order to more easily calculate the integral in Equation 2.36, we rearrange the integrand and apply the divergence theorem—

$$\hat{\boldsymbol{S}}_{\mathbf{1}}^{\boldsymbol{B}}=\int(\nabla\cdot\hat{\boldsymbol{\Pi}}_{\mathbf{0}})\cdot\boldsymbol{v}dV=\int\nabla\cdot(\hat{\boldsymbol{\Pi}}_{\mathbf{0}}\cdot\boldsymbol{v})dV-\int(\hat{\boldsymbol{\Pi}}_{\mathbf{0}}:\nabla\boldsymbol{v})dV,$$

$$\hat{\boldsymbol{S}}_{\mathbf{1}}^{\boldsymbol{B}}=-\int_{r=1}\boldsymbol{n}\cdot(\hat{\boldsymbol{\Pi}}_{\mathbf{0}}\cdot\boldsymbol{v})dA+\int_{r=\infty}\boldsymbol{n}\cdot(\hat{\boldsymbol{\Pi}}_{\mathbf{0}}\cdot\boldsymbol{v})dA-\int(\hat{\boldsymbol{\Pi}}_{\mathbf{0}}:\nabla\boldsymbol{v})dV. \quad (2.38)$$

The second term is zero because the integrand goes like $1/r^3$, and hence the integral can be neglected far from the particle. Thus, we have now determined expressions for all of the terms up to O(c) in Equation 2.10. The overall solution is summarized as—

$$\langle\hat{\boldsymbol{\sigma}}\rangle=\langle\hat{\boldsymbol{\tau}}_{\mathbf{0}}\rangle+\frac{nc}{De}\int_{r>1}\hat{\boldsymbol{A}}_{\mathbf{0}}'dV+\frac{c\hat{\tilde{\boldsymbol{A}}}_{\mathbf{0}}}{De}+n\hat{\boldsymbol{S}}_{\mathbf{0}}+nc\hat{\boldsymbol{S}}_{\mathbf{1}}^{\boldsymbol{A}}+nc\hat{\boldsymbol{S}}_{\mathbf{1}}^{\boldsymbol{B}}. \quad (2.39)$$

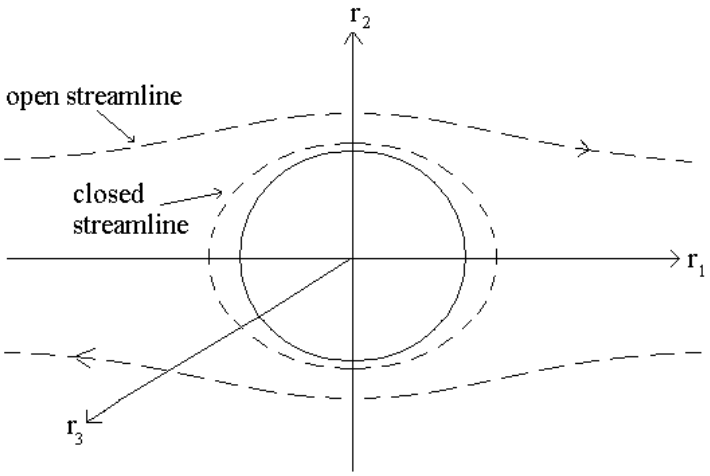

Figure 2.1: Different types of trajectories calculated with the computational method.

2.3.3 Computational Method

We now turn to the quantitative calculation of the bulk stress. We use a Runge Kutta four parameter equation in order to integrate the different systems of partial differential equations (including Equations 2.6 and 2.17, and the appropriate stress equations for each of the terms given in Equation 2.39). We convert one spatial dimension of the area or volume integrals into a time dimension by using the idea that the velocity of the fluid multiplied by the integral of a quantity over time is equivalent to the volume integral obtained using a finite control volume approach. Physically, in our case, this method of calculating the volume integral of the stress is equivalent to calculating the rate at which polymers enter the volume times the integral of their residence time in the volume. For a more rigorous proof, consider a quantity P that is equal to the time integral along a streamline of a quantity Q—

$$P = \int_{t-entry}^{t} Q\, dt', \tag{2.40}$$

where

$$Q = \frac{DP}{Dt} = \nabla \cdot (\boldsymbol{u}). \tag{2.41}$$

Performing a volume integral on both sides of Equation 2.41, we obtain—

$$\int Q dV = \int \nabla \cdot (\boldsymbol{u}P) dV. \tag{2.42}$$

Applying the divergence theorem,

$$\int Q dV = \int \boldsymbol{n} \cdot (\boldsymbol{u}P) dA. \tag{2.43}$$

Applying Equation 2.43 to the volume integrals in Equation 2.39, we obtain —

$$\int_{r>1} \hat{\boldsymbol{A}}'_{\mathbf{0}} dV = \int (\boldsymbol{n} \cdot \boldsymbol{u}) dA \int \hat{\boldsymbol{A}}'_{\mathbf{0}} dt = \int \boldsymbol{u}_{init} \cdot \boldsymbol{n} dA \int \hat{\boldsymbol{A}}'_{\mathbf{0}} dt, \tag{2.44}$$

where $\boldsymbol{u}_{init}$ is the velocity field at the starting point on the streamline trajectory.

The area integrals given by Equations 2.29 and the first term of 2.38 are calculated with a similar conversion, except that in this case, we solve the ODEs along a trajectory on the particle surface at the speed of the particle rotation rate, yielding (for the first term of 2.38)—

$$\int_{r=1} \boldsymbol{e_\phi} \cdot (\hat{\boldsymbol{\Pi}}_{\mathbf{0}} \cdot \boldsymbol{u}) dA = \int (\boldsymbol{e_\phi} \cdot \boldsymbol{u}) d\phi \int \boldsymbol{e_\phi} \cdot (\hat{\boldsymbol{\Pi}}_{\mathbf{0}} \cdot \boldsymbol{u}) dt = \int \omega sin(\theta) d\phi \int \boldsymbol{e_\phi} \cdot (\hat{\boldsymbol{\Pi}}_{\mathbf{0}} \cdot \boldsymbol{u}) dt. \tag{2.45}$$

where ω is the rotation speed of the sphere. Streamlines for open and closed loop trajectories must be calculated (see Figure 2.1). For the closed streamlines, the integration is performed over loops that begin at $r_2 = 0$ for all r_1 and r_3. As the equilibrium state of the polymer conformation tensor is unknown at the beginning of the closed loop, we must integrate around the closed loop trajectory multiple times in order to determine a steady state solution where two successive loops give the same value of the integral around the particle. Due to the system symmetry, the calculation for the positive r_3 values is performed and the numerical results

are multiplied by 2 to obtain the overall integral. For the open streamlines, the integration is performed on streamlines that begin at $r_1 \ll 0$, for all r_2 and r_3. As with the closed streamlines, symmetry is used to simplify the calculation, which is performed only for positive r_2 and r_3 values. The final result is obtained by multiplying the numerical results by 4.

It should be noted that an additional type of integration must be performed in order to solve Equation 2.27. In that case, we solve Equation 2.25, integrating from a point far from the particle along an undisturbed velocity streamline in order to find $\hat{\boldsymbol{A}}_{\boldsymbol{0}}^{\boldsymbol{L}}$ at the point of interest. To make the calculation tractable, a grid of $\hat{\boldsymbol{A}}_{\boldsymbol{0}}^{\boldsymbol{L}}$ points is found before integrating $\hat{\boldsymbol{A}}_{\boldsymbol{0}}^{\boldsymbol{\prime}}$, and a 3D interpolation is performed for each point.

In all cases, solutions for characteristic curves are found at increasing distances from the particle center until the contributions are negligible.

Convergence

Several types of convergence had to be achieved in order to yield an accurate computational result. First, the spatial and time steps had to be sufficiently small. Second, for the closed loops, the integration along a streamline was repeated until the different values of the integral along two successive loops was within the specified tolerance (less than 0.1% error). Third, for the integrals along the open streamlines, the domain size was required to be large enough to capture the entire volume integral.

A principal limitation in the convergence of the contribution from the extra polymer stress is the integration of $\boldsymbol{A}_{\boldsymbol{0}}^{\boldsymbol{L}}$. The grid of points determined from the

Table 2.1: Comparison between Oldroyd-B and 2nd order fluid results in the limit of low De.

Quantity	Oldroyd-B	2nd Order Fluid
$\Pi_{0,11} - \Pi_{0,22}$	$0.002\pi De$	0
$\Pi_{0,22} - \Pi_{0,33}$	$2.24\pi De$	$2.38\pi De$
$S^A_{1,12} + S^B_{1,12}$	3.31π	3.33π
$S^A_{1,11} - S^A_{1,22}$	$3.96\pi De$	$4.00\pi De$
$S^A_{1,22} - S^A_{1,33}$	$-1.98\pi De$	$-2.00\pi De$
$S^B_{1,11} - S^B_{1,22}$	$2.67\pi De$	$2.67\pi De$
$S^B_{1,22} - S^B_{1,33}$	-0.142πDe	-0.143πDe

integration of $\boldsymbol{A_0^L}$ were calculated and stored so that they could be interpolated when the overall equation was solved, and thus there was a computational limit based on the number of points that could be stored in memory. While this memory limitation posed no problem for open streamlines, which could be broken up into many smaller volumes, the closed streamlines required a large volume of calculation and also required a finer mesh due to their proximity to the particle, where the flow field is changing more rapidly than for the streamlines far from the particle.

The volume of integration used for the calculations was 160^3 for the stresslet calculation and 80^3 for the average polymer stress calculation. For the stresslet calculation, doubling the volume from 40^3 to 80^3 yielded a less than 0.1% change in the both of the normal stress differences at the highest De. For the average stress calculation, doubling the volume from 40^3 to 80^3 yielded a 9.6% decrease in the first normal stress difference and a 0.3% increase in the second normal stress difference at the highest De.

2.3.4 Comparison

In order to verify the computational results, we compare each term in the limit of low De to the terms obtained by Koch & Subramanian [10] in their second-order fluid study. The overall result, written in terms of De for the Oldroyd-B fluid, from Koch & Subramanian [10] is

$$N_1 = \frac{20}{3}\pi De$$
$$N_2 = \frac{5}{21}\pi De, \tag{2.46}$$

where N_1 and N_2 are the first and second normal stress differences, respectively, and are related to the normal stress difference coeffecients by $N_1 = \psi_1\dot{\gamma}^2$ and $N_2 = \psi_2\dot{\gamma}^2$. It should be noted that the definition of De is different in the second-order fluid constitutive equation, defined in terms of the first normal stress difference as $De_{2nd-order} = \psi_1^0\dot{\gamma}/\eta_0$, where η_0 is the zero shear rate viscosity, rather than the Hookean spring relaxation time. The two equations can be compared directly using an appropriate parameter choice to make the second normal stress difference in the fluid equal to zero. The results of the comparison are shown in Table 2.1. As can be seen, the results match very well, with all simulation results within 5% of the theoretical results for the different contributions to the suspension stress.

2.3.5 Results and Discussion

Figures 2.2, 2.3, and 2.4 show the overall results for the shear stress and normal stress differences due to the addition of polymer to the suspension as a function of De, scaled with the particle concentration ϕ. As can be seen, the shear stress and first normal stress increase with increasing De, while the second normal stress difference decreases slightly with increasing De. Since the stresses are

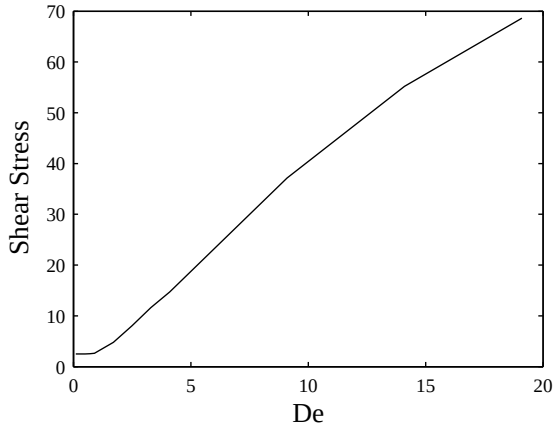

Figure 2.2: Overall non-Newtonian shear stress as a function of De.

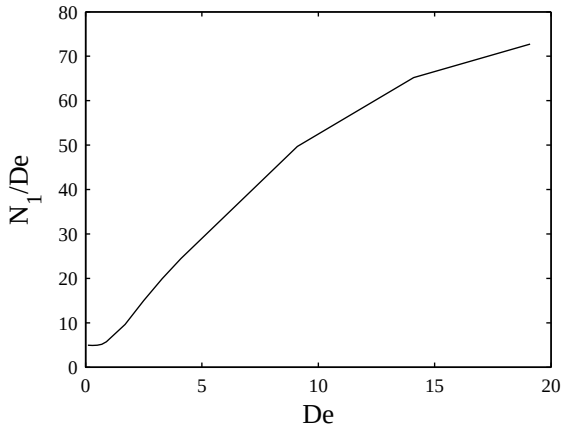

Figure 2.3: Overall first normal stress difference as a function of De.

non-dimensionalized with shear rate, the non-dimensional shear stress is a scaled viscosity, and the non-dimensional normal stress differences divided by De are scaled normal stress difference coefficients. In order to gain a more physical understanding of the nature of the polymer-particle interactions, we examine the contributions of the individual components of the different rheological properties of the suspension. Figures 2.5–2.9 give the individual contributions to the shear stress, the first normal stress difference divided by De, and the second normal stress

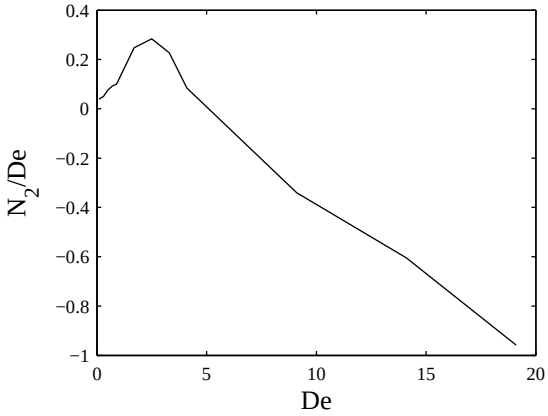

Figure 2.4: Overall second normal stress difference as a function of De.

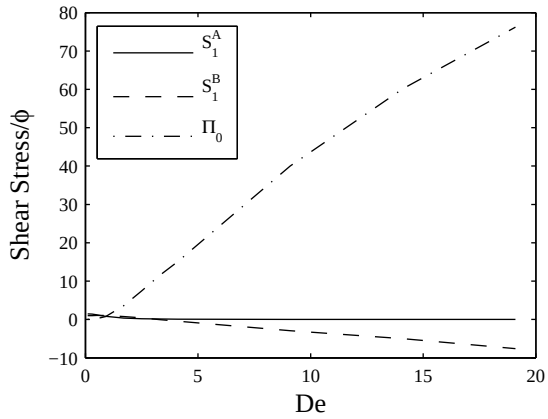

Figure 2.5: Contributions to the non-Newtonian shear stress.

difference divided by De. First, we consider the contributions due to leading order polymer stress tensor (Π_0). At low De, the shear stress grows with De^2, as would be expected based on the asymptotic ordered fluid expansion. Considering only the 1 and 2 directions, there are deviations from the constant Newtonian viscosity at third order, when there are shear components arising from the terms cubic in the rate of strain tensor. Similar arguments can be made for the first and second normal stress differences. The normal stress difference coefficients are predicted to be constants at second order. Third order terms only contribute to the shear

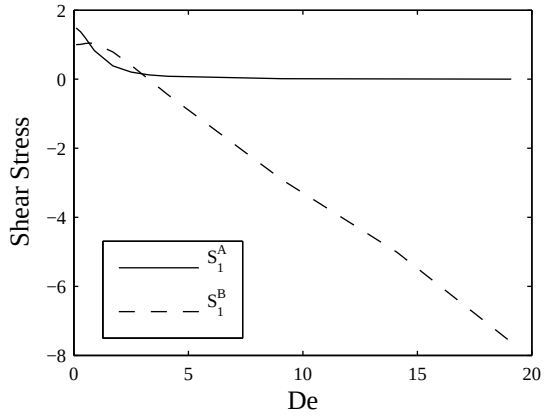

Figure 2.6: Stresslet contributions to the non-Newtonian shear stress.

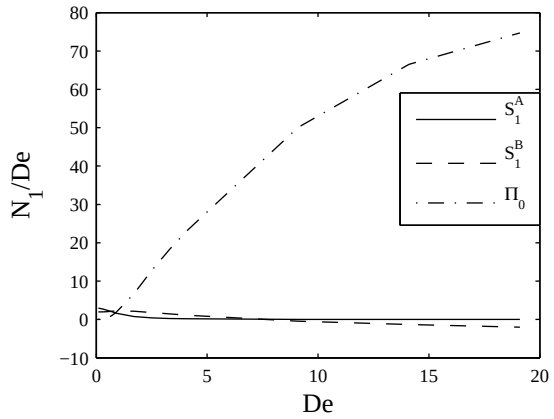

Figure 2.7: Contributions to the first normal stress difference.

stress, but at fourth order (with terms quartic in the rate of strain tensor), there are contributions proportional to De. Thus, we expect quadratic scaling at low De for the normal stress coefficients as well. This scaling is observed for the first normal stress difference coefficient. The second normal stress difference coefficient appears to decrease linearly at low De.

Koch & Subramanian [10] proposed that at finite De the first normal stress difference due to the polymers near the particle is enhanced due to the fluid rotation

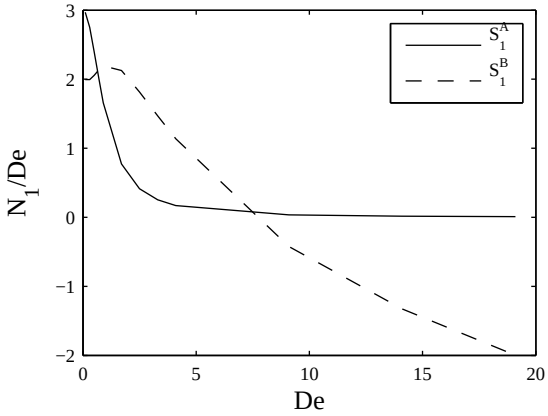

Figure 2.8: Stresslet contributions to the first normal stress difference.

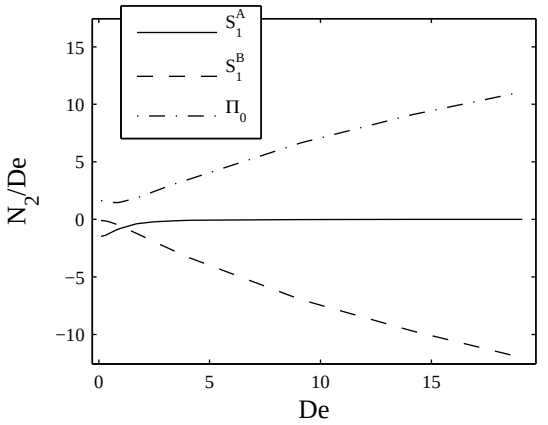

Figure 2.9: Contributions to the second normal stress difference.

near the particle. They noted that at leading order, the polymers align in the extensional axis of the mean extension rate, which is 45 degrees to the 1 and 2 axes in the case of a simple shear flow. Then, the rotational field near the particle both rotates and translates the polymers such that the 11 component of the stress is significantly enhanced near the particle. A close examination of the flow fields in our Oldroyd-B calculations in this study shows that this indeed occurs. Figures 2.11 and 2.12 show the evolution of the polymer conformation tensor along an open streamline. As is seen, the polymers rotate when they approach the

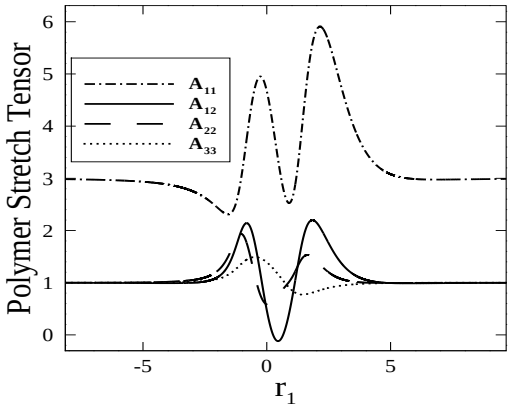

Figure 2.10: Components of the polymer conformation tensor $\boldsymbol{A}$. Open streamline starting at r_1=-200, r_2=0.5, r_3=0. $De = 1$.

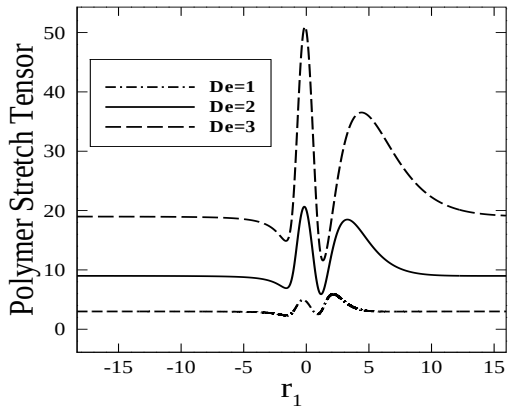

Figure 2.11: 11 component of the polymer conformation tensor $\boldsymbol{A}$ at different De. Open streamline starting at r_1=-200, r_2=0.5, r_3=0. $De = 1$.

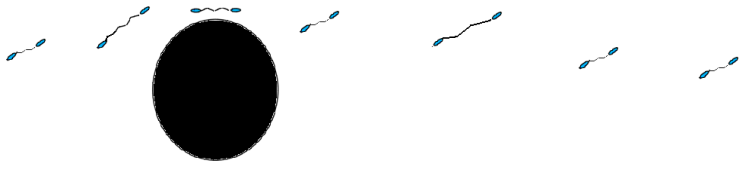

Figure 2.12: Evolution of polymer at $De = 1$. Open streamline starting at r_1=-200, r_2=0.5, r_3=0.

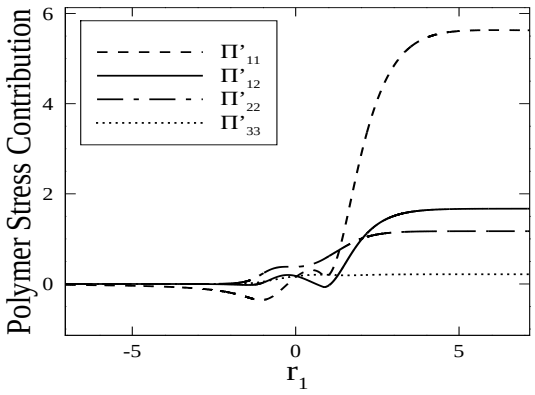

Figure 2.13: Integral of $\mathbf{\Pi'}$ along a streamline starting at r_1=-200, r_2=0.5, r_3=0. $De = 1$.

particle, and the 12 and 22 components of the stress are enhanced while the 11 component decreases. As the polymers continue approaching the particle, they translate and rotate with the flow around the particle, and the 11 component has a large peak near $r_1 = 0$. On the downstream side of the particle, some of the polymer stress is rotated to the 12 and 22 direction, and Figure 2.10 shows a second peak for these components. As the polymers leave the region near the particle, the flow rotates and translates them again, realigning the polymers with the flow direction, where the 11 component has a second peak before the polymer relaxes to its equilibrium length for the simple shear flow. This description of the polymer behavior explains the observed contributions to the bulk stress from the polymer, including the contribution from the alteration of the polymer stress field due to the particle velocity disturbance and the polymer stress contribution to the particle stresslet. The particle disturbance flow enhances the 12 component of $\hat{\boldsymbol{A}}$, leading to increasing shear stress. It also enhances the 11 and 22 components, although the 11 component is enhanced to a greater degree, leading to positive, increasing contributions to both normal stress differences. The components of the conformation tensor are enhanced for higher De, with both larger peaks and longer

relaxation times.

Figure 2.13, which plots the total integral of different components of $\mathbf{\Pi'}$ as a function of r_1, the largest contributions to the different components of $\hat{\boldsymbol{A}}$ occur after the polymers have passed the particle. The disturbance velocity stretches the polymer to a longer length than the equilibrium length in shear flow and the particle disturbance flow rotates and translates the polymer to an orientation that is aligned with the flow direction, with the 22, then 12, and lastly 11 components of the polymer contributions due to the particle disturbance to the bulk suspension stress all increasing. It is of note that the observations here are in agreement with Harlen & Koch [5], who found that this transferral of stress due to disturbance velocity fields was seen in the case of a fiber in a low concentration polymer suspension and also observed an enhancement of the same evolution of the 22 component to 11 component of the polymer conformation near a fiber.

Next we consider the stresslet contributions to the suspension stress. In the limit of $De = 0$, the total stress (derived from the two parts of the stresslet) matches the Einstein result in Equation 2.28. The contribution due to the Newtonian disturbance flow acting on the polymers ($\boldsymbol{S_1^A}$) is equal to $\frac{8\pi}{3}\tilde{e}_{12}$ and the contribution due to the alteration of the Newtonian velocity field by the polymers ($\boldsymbol{S_1^B}$) is equal to $4\pi\tilde{e}_{12}$. On the surface of the particle, the polymer gives a much smaller contribution to the particle stresslet ($\boldsymbol{S_1^A}$). For this case, the streamlines are simply circles around the sphere surface, and in the rotating reference frame, the polymer sees an oscillating shear flow. At lower $De < 0.3$, the polymer stress grows as the second-order fluid equation would predict; the normal stress differences scale with De, and the shear stress is a constant. However, at higher De, the polymer stresses actually go to zero, with the normal stress differences scaling with $1/De$ and the shear stress scaling with $1/De^2$. To understand this behavior, first it

should be noted that the mean shear rate in the $r\phi$ direction is zero, which can be determined by integrating the gradient of Equation 2.17 in spherical coordinates over $0 < \phi < 2\pi$ and $r = 1$. From this zero mean shear rate, the polymer stresses would not be expected to grow with De at high De. Instead, the components of $\hat{\boldsymbol{A}}$ oscillate with the oscillating shear flow, at first out of phase but asymptotically becoming in phase. The out of phase nature of the two oscillations gives small normal stresses; the shear stress, on the other hand, has no net contribution to the polymer stress from the leading order conformation tensor due to symmetry of the 12 component of $\boldsymbol{A}$.

The stresslet contributions due to the alteration of the Newtonian flow field by the polymers ($\boldsymbol{S_1^B}$) oppose the contributions due to the alteration of the polymer stress by the leading order disturbance flow field ($\boldsymbol{\Pi_0}$). The $\boldsymbol{S_1^B}$ contributions to the shear stress and first and second normal stress differences are all negative, in contrast to the positive contributions from the $\boldsymbol{\Pi_0}$ term. These opposing contributions arise because the polymer resists the particle disturbance flow field, thus weakening the Newtonian flow. Their effects are not as strong for the cases of the shear stress and the first normal stress difference, but are slightly stronger for the case of the second normal stress difference.

In summary, the rheological properties of particle suspensions are significantly altered at high De, with the shear stress and first normal stress difference divided by De growing with De and the second normal stress difference divided by De decreasing with De for $De > 4$. The principal contributions at higher De to the different rheological properties are 1) the extra polymer stress due to the Newtonian particle disturbance flow field and 2) the Newtonian stresslet contribution due to changes in the Newtonian velocity field by the polymers. These two contibutions are of opposite sign, with the latter being caused by a resistance to the

Table 2.2: Fitted equations to simulation data for different rheological properties. Maximum error is less than 1% for all equations.

Quantity	Fitted Equation	Range
N_1/De	$(21.4589 - 3.8607De + 3.0064De^2)\phi$	$De \leq 1$
N_2/De	$(0.6495 + 1.1271De - 0.8280De^2)\phi$	$De \leq 1$
Shear Stress	$(10.4835 + 0.2496De + 2.2712De^2)\phi$	$De \leq 1$
N_1/De	$(-13.7539 + 22.7277De - 0.2994De^2)\phi$	$De > 1$
N_2/De	$(1.6713 - 0.4101De + 0.0055De^2)\phi$	$De > 1$
Shear Stress	$(-8.5448 + 15.0821De - 0.1960De^2)\phi$	$De > 1$

former. The results presented here extend the theory of non-Newtonian suspension rheology to include polymers that have large relaxation times, a system common in practice. It would be of great interest to have experimental measurements with non-shear thinning Boger fluids at a range of De to verify the elastic polymer behavior predicted by this work. Equations fitted to the simulation data for the different rheological properties are given in Table 2.2 for two different ranges of De, which can be used to compare with experimental data. While some experimental work predicting the suspension stress for spheres in a polymeric solvent has been performed, experimental studies to date have used fluids whose properties change based on De, making it a a prohibitive task to separate the pure fluid effects of the suspension from the particle-polymer interactions due to finite polymer relaxation time.

REFERENCES

[1] H. Barnes. A review of the rhelogy of filled viscoelastic systems. In *Rheology Reviews*, pages 1–36. 2003.

[2] G.K. Batchelor. The stress system in a suspension of force-free particles. *J. Fluid Mech.*, 41:545–570, 1970.

[3] K. Desai and H. Park. Recent developments in microencapsulation of food ingredients. *Drying Technology*, pages 1361–1394, 2005.

[4] F. Greco, G. D'Avino, and P.L. Maffettone. Rheology of a dilute suspension of rigid spheres in a second order fluid. *J. Non-Newt. Fluid Mech.*, 147:1–10, 2007.

[5] O.G. Harlen and D.L. Koch. Orientational drift of a fibre suspended in a dulute polymer solution during oscillatory shear flow. *J. Non-Newtonian Fluid Mech.*, 73:81–93, 1997.

[6] D. Highgate and R. Whorlow. Rheological properties of suspensions of spheres in non-newtonian media. *Rheol. Acta*, 9:569–576, 1970.

[7] W. R. Hwang, M. A. Hulsen, and H. E. H. Meijer. Direct simulations of particle suspensions in a viscoelastic fluid in sliding bi-periodic frames. *J. Non-Newt. Fl. Mech.*, 121:15–33, 2004.

[8] D. Jin and J. Ding. Rheology of a polymer-based hybrid suspension composed of concentrated poly[(d,l-lactide)-co-glycolide] solution and inorganic salt particles. *Macromolecular Bioscience*, 2007.

[9] P. N. Kaloni and V. Stastna. Steady-shear rheological behavior of the suspension of spherical particles in a second-order fluid. *Polym. Eng. Sci.*, 23:465, 1983.

[10] D.L. Koch and G. Subramanian. The stress in a dilute suspension of spheres suspended in a second-order fluid subject to a linear velocity field. *J. Non-Newt. Fluid Mech.*, 138:87–97, 2006.

[11] M.K. Lyon and L.G. Leal. An experimental study of the motion of concentrated suspensions in two-dimensional channel flow. Part I. *J. Fluid Mech.*, 363:25–56, 1998.

[12] R. T. Mifflin. Dissipation in a dilute suspension of spheres in a second-order fluid. *J. Non-Newt. Fl. Mech.*, 17:267, 1985.

[13] A. Nasu and Y. Otsubo. Rheology and UV-protecting properties of complex suspensions of titanium dioxides and zinc oxides. *J. Coll. Interface Sci.*, 310:617–623, 2007.

[14] N. A. Patankar and H. H. Hu. Rheology of a suspension of particles in viscoelastic fluids. *J. Non-Newt. Fl. Mech.*, 96:427–443, 2001.

[15] X. Qin, M.R. Thompson, and A.N. Hrymak. Rheology studies of foam flow during injection mold filling. *Poly. Eng. Sci.*, 47:522–529, 2007.

[16] K. Sun and K. Jayaraman. Bulk rheology of dilute suspensions in viscoelastic liquids. *Rheol. Acta*, 23:84–89, 1984.

[17] I. Zarraga, D. Hill, and D. Leighton. The characterization of the total stress of concentrated suspensions of noncolloidal spheres in newtonian fluids. *J. Rheol.*, 44:185–220, 2000.

[18] I. Zarraga, D. Hill, and D. Leighton. Normal stresses and free surface deformation in concentrated suspensions of noncolloidal spheres in a viscoelastic fluid. *J. Rheol.*, 45:1065–1084, 2001.

Chapter 3

Cross-stream forces and velocities of fixed and freely suspended particles in viscoelastic Poiseuille flow: Perturbation and numerical analyses

3.1 Summary

The cross-stream migration of circular particles (or infinitely long cylinders) in two dimensional viscoelastic pressure-driven flows is examined through complementary second-order fluid perturbation analyses for small Deborah number (De), where De is defined as the fluid relaxation time divided by the characteristic flow time, and Oldroyd-B fluid finite element simulations. A neutrally buoyant, freely suspended particle is found to migrate toward the center of the channel for all particle sizes and cross-stream positions due to the coupled effects of the linear and quadratic variations of the imposed velocity. A particle that is held at a fixed position, on the other hand, experiences a cross-stream force directed toward the wall as a result of the coupled effects of the local shear flow and the flow relative to the particle.

3.2 Introduction

Particles migrate in viscoelastic suspensions to preferred cross-stream positions due to external surface forces perpendicular to the fluid streamlines. These forces occur due to inhomogeneous velocity and/or temperature fields that alter fluid properties near the particle. As a result of particle migration, inhomogeneous

suspensions form that can have significantly different rheological properties, with consequences for processing applications such as injection molding. These applications have motivated several studies that have looked at the forces acting on a particle suspended in a viscoelastic Poiseuille flow, but the previous literature has not shown a clear result for the parameters that affect the direction and magnitude of the cross-stream force on a particle. No study to date has included an extensive comparison of quantitative simulation and analytical results, which is of great value in a topic with contradictory findings on even the most fundamental qualitative result of the migration direction. In light of this, the current study develops a full 2D theory to predict the cross-stream force and migration velocity for a particle in a Poiseuille flow at low De, for both a particle moving with the fluid and a particle fixed in place. Trajectories for a freely suspended particle at low De are computed based on the analytical predictions. Finite element method (FEM) simulations balance a cross-stream body force with the migration force in order to validate the perturbation analysis results in the appropriate asymptotic limits and to perform a parametric study examining the effects of De, particle size, particle location, and polymer concentration.

Previous theory-based attempts to explain the migration phenomenon have examined the fluid-particle interactions of stress and velocity fields (e. g. [1],[14],[18]). In an inertia-less flow, migration in a dilute suspension is only predicted to occur in non-Newtonian fluids; with these types of suspending fluids, particles are predicted to migrate preferentially to either the wall or the center of a bounded flow, depending on system conditions. Ho & Leal [6] studied the particle migration of a sphere through a small De perturbation analysis in a second-order fluid. They derived an expression for the cross-stream migration force on a small particle (radius$\ll$channel height) in Poiseuille flow, finding that the particle always migrates to the center of

the channel. They found that the migration force is a function of the ratio of the particle size to the channel height, the position of the particle, and the first and second normal stress differences. Ho & Leal [6] also investigated circular Couette flow, finding that particles migrate to the outer wall, where the absolute shear rate is at a minimum.

Several numerical studies have also addressed the pheonomenon of particle migration. Carew & Townsend [4] found in their finite element simulations that a fixed cylinder in a Poiseuille flow has a cross-stream force toward the wall in both Oldroyd-B and Phan-Thien-Tanner fluids. Huang, Hu, & Joseph [7] also performed Oldroyd-B FEM simulations on a cylindrical particle in a Poiseuille flow, although the particle was allowed to move with the fluid. They found that the direction of the cross-stream force depended on the particle size. While their simulation conditions are the most similar to those in this study, their method differs significantly in that they determined the actual motion of the particles by simulating the trajectory of the particles based on surface forces at each time step. In contrast, a trajectory cannot be plotted from the simulation results in the present study (although analytical trajectories are presented). Rather, the cross-stream migration tendency is determined by examining the stresses normal to the channel walls acting on a particle that is fixed in the cross-stream direction. While Huang et al. 's approach does provide the advantage of showing the particle trajectory, the principal disadvantage is that since the initial condition for the particle is a zero-velocity, zero-rotation condition, there is a transient period where the particle does not have the proper force-free, torque-free boundary condition. Their results primarily addressed flows with finite De and finite Reynolds number (Re), defined as uH/ν, where u is the characteristic velocity, H is the channel height, and ν is the kinematic viscosity. When they addressed the low Re limit,

they omitted the nonlinear inertial term in the Navier-Stokes equation, but kept the transient particle and fluid inertia; thus, not all inertia was neglected. They found that larger particles migrated toward the wall and smaller particles migrated toward the center. Thus, although two computational studies have been performed, there are no studies that have modeled freely suspended particles in inertia-less shear flows, the emphasis of this study and often the system of interest for theory and experiments, as well as applications requiring high viscosity fluids and/or small particles.

No experimental studies to date have exactly mimicked the conditions of the previous analytical and numerical studies. Nevertheless, several investigators have studied particles in creeping, viscoelastic Poiseuille flows, finding contrasting results for the direction of the cross-stream force. Karnis and Mason [11] did some of the first work on a highly concentrated (particle weight fraction of 0.125) suspension of spheres in a shear thinning polymer solution, finding the spheres migrated to the center of a pipe, regardless of their initial position. More recently, Jefri and Zahed [10] found that spherical particles in a constant viscosity suspension migrated toward the center plane, while particle in shear-thinning fluids migrated toward the plates (or walls) of the channel in a creeping Poiseuille flow. They used a particle volume fraction of 0.02, so there were some hydrodynamic particle-particle effects in the system, with most particles aggregating into short chains of 2-10 particles. However, even though Jefri and Zahed's study examined multiple particles rather than a single particle, their work provides a good source of qualitative comparison in the experimental realm because they performed experiments in the appropriate particle size limit and flow regime of the perturbation analysis of Ho & Leal [6]. In contrast to the results of Jefri and Zahed [10], Dhahir and Walters [5] found that a fixed, freely rotating single cylinder felt a cross-stream

force toward the channel wall in Poiseuille flow conditions for both Boger and pseudoplastic fluids. The experimental data from Dhahir & Walters [5] for a fixed particle in a suspending Boger fluid will be compared with FEM simulation results obtained in this study.

In summary, the past investigations have come to varied conclusions on the direction of particle migration in a non-Newtonian Poiseuille flow. While perturbation analyses indicate that a particle always experiences a cross-stream force toward the channel center, some simulations and experiments have shown a cross-stream force in the opposite direction. The only explanation for the switch in cross-stream force direction that has been advanced is that particle size is the main parameter affecting the cross-stream force direction. We do not reach the same conclusion and find that in fact the direction of the cross-stream force is related to the boundary condition on the particle. We hope to clear up the discrepancies in the literature in this 2D perturbation analysis and computational study through a detailed study of the flow and stress profiles on the surface of the particle and a thorough examination of the effects of flow geometry, fluid parameters, and the particle boundary condition on the particle cross-stream force. The 2D perturbation analysis will allow for a direct comparison between analytical and numerical work. This was previously not possible since all of the theoretical work has been in 3D while the previous numerical work has been in 2D. The theory of Ho and Leal [6] for migration of a spherical particle at low Deborah number in a Poiseuille flow required an application of the generalized reciprocal theorem to obtain the cross-stream force without an explicit determination of the perturbed fluid velocity and pressure field. However, particle-wall hydrodynamic reflections could be neglected to leading order for small particle sizes. In contrast, the Tanner-Pipkin theorem allows us to determine the cross-stream force on a circular particle without appli-

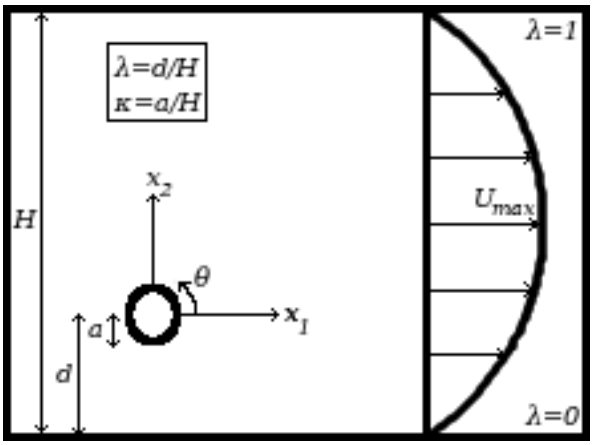

Figure 3.1: Diagram of the flow situation.

cation of the generalized reciprocal theorem. The Tanner-Pipkin theorem states that the Newtonian and second-order fluid velocity fields are the same in a two-dimensional flow and it provides a prescription for the perturbed pressure field. In the two-dimensional problem, hydrodynamic particle-wall interactions are important in evaluating the migration velocity of a particle owing to the logarithmic nature of the fluid velocity produced by a translating cylinder.

In the first section, we will outline the system in consideration, a description of the problem, and the methodology for solution. In the next section, we will present the derivation of the expressions for the cross-stream force and velocity for a freely suspended particle along with complementary FEM simulations results. In the last section, we will derive the cross-stream force for a fixed particle and compare the expression to previous experimental results from the literature. We will also present complementary FEM simulation results, and the effects of extending various parameters past the analytical limits will be explored.

3.3 Approach

The system under consideration is a 2D cylinder in a creeping pressure-driven (Poiseuille) planar flow, with an imposed velocity field that remains parabolic at all De for both the analyses and simulations due to the choices of non-shear thinning constitutive equations. Figure 3.1 shows a diagram of the situation with the variables that will be used in the derivations and discussion that follow.

The overall goals of the analytical part of this study are to (1) find expressions for the cross-stream force acting on a particle in Poiseuille flow for both freely suspended and fixed boundary conditions, (2) find an expression for the migration velocity of a freely suspended particle in Poiseuille flow, and (3) understand the mechanism by which the migration velocity and cross-stream forces arise. The numerical work complements the perturbation analysis by verifying the analytical predictions in the appropriate limits and extending the results to perform a parametric study for the cross stream force on both a freely suspended and a fixed particle.

In the analyses that follow, we use the second-order fluid constitutive equation to perform perturbations about $De = 0$. For this constitutive equation, the Tanner-Pipkin theorem [3] states that the $\mathrm{O}(De)$ contribution to the velocity field is zero and gives an analytical expression for the non-Newtonian pressure. In the case of the FEM simulations, the Oldroyd-B constitutive equation is employed, which allows us to calculate high De results.

Due to the complexities of a deformable mesh code, we consider a single, unchanging mesh for a given particle/channel geometry. In order to simulate the flow field, a Galilean transformation is performed by adding a uniform velocity field in

the opposite direction of the pressure gradient which ensures no net force on the particle in the streamwise direction. In contrast, the particle does experience a force in the cross-stream direction, but since the particle is not allowed to move, this is physically equivalent to a particle translating in a channel with some external body force acting on it in the cross-stream direction, such as gravity in a horizontal channel.

3.3.1 Analysis

We first consider the case of a freely suspended cylinder in a Poiseuille flow that does not move in the x_2 direction due to a body force equal in magnitude to the cross-stream migration force. For the analysis of this case, we first write the Cauchy momentum equation and continuity equation for Newtonian creeping flow—

$$\boldsymbol{\nabla \cdot \tau} = 0, \quad \boldsymbol{\nabla \cdot u} = 0, \tag{3.1}$$

where $\boldsymbol{\tau}$ is the fluid stress tensor and $\boldsymbol{u}$ is the fluid velocity. We then perform a multipole expansion of the fluid stress tensor in the preceding equation in order to find the Newtonian flow field. Next, we find the non-Newtonian stress and flow fields by employing the second-order fluid constitutive equation, which is derived by a "retarded motion" expansion of the Newtonian fluid stress for powers of the rate of strain tensor and its convected derivative. This constitutive equation describes all fluids at small De but deviates from experimental data at finite shear rate and/or polymer relaxation time. The second order terms describe elastic polymer stresses but do not model shear-thinning effects, which arise at third order. However, since De is a small parameter, the effects of shear thinning are expected to be small in the analytical cases examined. The stress is written as—

$$\boldsymbol{\tau} = 2\kappa \boldsymbol{e} - 2De \left[\frac{\partial}{\partial t} \boldsymbol{e} + \boldsymbol{u} \cdot \nabla \boldsymbol{e} - \boldsymbol{e} \cdot \boldsymbol{\omega} + \boldsymbol{\omega} \cdot \boldsymbol{e} \right] + 8 \frac{\psi_2}{\psi_1} De \, \boldsymbol{e} \cdot \boldsymbol{e}, \tag{3.2}$$

where

$$\boldsymbol{e} = \frac{1}{2}\left(\nabla \boldsymbol{u} + \boldsymbol{u}^T\right), \tag{3.3}$$

$$\boldsymbol{\omega} = \frac{1}{2}\left(\nabla \boldsymbol{u} - \boldsymbol{u}^T\right), \tag{3.4}$$

η_0 is the zero shear viscosity, and ψ_1 and ψ_2 are the first and second normal stress coefficients, respectively. In the preceding equations, the variables are non-dimensionalized by a combination of the characteristic force per length ($\eta_0 U_{max}$), time (H/U_{max}), and length (a) scales. These scaling choices give order 1 parameters near the particle; for example, the stress is non-dimensionalized by $\eta_0 U_{max}/a$, which is the viscous stress on the particle surface.

The Deborah number is defined as the relaxation time λ_r of the fluid multiplied by the absolute value of the average rate of strain in the undisturbed flow—

$$De = \frac{U_{max}\lambda_r}{H}, \tag{3.5}$$

where

$$\lambda_r = \frac{\psi_1}{2\eta_0}. \tag{3.6}$$

Note that the choice of characteristic flow time ensures that De is constant for all positions in the channel; however, the local rate of strain and characteristic fluid time are not constant, changing based on x_2. Most of the parametric study results are at a position $\lambda = 0.416667$, which has a local rate of strain that is 1.5 times lower than the mean rate of strain.

The velocity, pressure, and stress are expanded in small De, with effects up to order De considered—

$$\boldsymbol{u} = \boldsymbol{u^{(0)}} + O(De^2), \tag{3.7}$$

$$p = p^{(0)} + De\, p^{(1)} + O(De^2), \tag{3.8}$$

$$\boldsymbol{\tau} = \boldsymbol{\tau^{(0)}} + O(De^2). \tag{3.9}$$

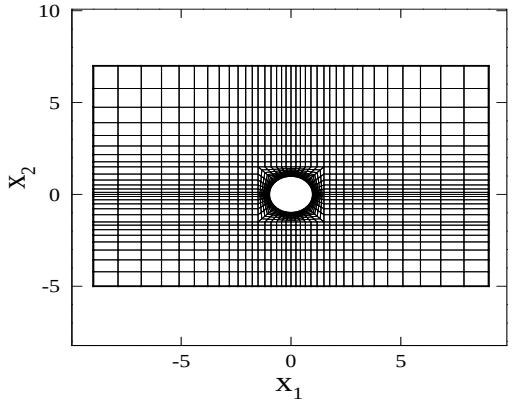

Figure 3.2: Typical FEM mesh.

The Tanner-Pipkin theorem specifies that the velocity field of a planar flow for the second-order fluid is the same as the one found in the Newtonian fluid, and thus the O(De) velocity and shear stress terms are zero. The second-order fluid pressure is determined by substituting the Newtonian pressure expression (Equation 3.16) into the Tanner-Pipkin pressure, given by Bird, Armstrong & Hassager [3] as

$$p = p^{(0)} - \frac{De}{\kappa}\frac{D}{Dt}p^{(0)} + \left(4\frac{\psi_2}{\psi_1} + 1\right) De(\boldsymbol{e}^{(\mathbf{0})} : \boldsymbol{e}^{(\mathbf{0})}). \tag{3.10}$$

In summary, to find the cross-stream force, we must find the Newtonian velocity and pressure fields with Equation 3.1 and the non-Newtonian pressure field with Equation 3.10 and then integrate the stress from Equation 3.2 on the surface of the particle.

3.3.2 Finite element simulations

FEM simulations of a cylinder in a Poiseuille flow are performed in order to validate the analytical predictions in the appropriate limits, as well as to extend the results to parameters outside of the validity of the analysis. The finite element method is a

computational approach that is used to find solutions to boundary-value problems, essentially discretizing the overall domain into a series of sub-domains, and solving appropriate equations for each element within this mesh. These equations are weighted along each element, and the overall error in each element is minimized such that the solution satisfies the governing equations over the entire domain. A good description of the method can be found in [2] or [8]. Figure 3.2 shows a mesh with the typical refinement used, although most of the meshes in this study have a larger height and longer length. The number of elements for the different meshes used ranges from 1,488–5,328, and the number of unknowns ranges from 26,065–92,281.

The FEM formulation solves a time-dependent problem, employing a 4th order Runge-Kutta method for time integration [15] and a DEVSS-G/SUPG spatial discretization [12]. A principal advantage of the code is its use of operator splitting, which splits the momentum equation and the constitutive equation, decoupling the stress term. The code simultaneously solves the Cauchy momentum, conservation of mass, and constitutive equations for each element.

The FEM simulations use an Oldroyd-B constitutive equation—

$$\boldsymbol{\tau} + (1-\beta)De\,\boldsymbol{\tau}_{(1)} = -(1-\beta)\kappa\left(\nabla\boldsymbol{u} + \nabla\boldsymbol{u}^T\right), \tag{3.11}$$

where

$$\boldsymbol{\tau}_{(1)} = \frac{\partial\boldsymbol{\tau}}{\partial t} + \boldsymbol{u}\cdot\nabla\boldsymbol{\tau} - \left(\nabla\boldsymbol{u}^T\cdot\boldsymbol{\tau} + \boldsymbol{\tau}\cdot\nabla\boldsymbol{u}\right) \tag{3.12}$$

and β is the ratio of solvent viscosity (η_s) to zero shear rate viscosity (η_0). The definition of De^{OB} for the Oldroyd-B fluid usually differs because the relaxation time is solely defined by the polymer, whereas the second-order fluid De relaxation time (Equation 3.6) is defined in terms of both the polymer and solvent. The

relationship between De^{OB} and the second-order fluid De is as follows—

$$De^{OB} = \frac{De}{1-\beta}. \tag{3.13}$$

For consistency, the second-order fluid De definition is used throughout the discussion, except where noted. The Oldroyd-B fluid has an advantage over the second-order fluid in that it can capture high deformation rates. It successfully models a class of fluids known as Boger fluids, which are non-Newtonian fluids that are created by dissolving a low concentration of high molecular weight polymer in a highly viscous fluid. These fluids exhibit constant viscosity over all shear rates and thus are useful in isolating elastic effects of a polymeric solution. Since the Oldroyd-B constitutive equation can predict high shear rate behavior, we can perform finite De simulations to expand upon the predictions of the second-order fluid analysis. It should be noted that many polymeric fluids exhibit a departure of the first normal stress difference from the quadratic scaling with the shear rate or a departure from constant shear viscosity at high shear rates, and for these solutions, the Oldroyd-B equation is accurate only in the low shear rate region. The second normal stress difference for an Oldroyd-B fluid is equal to zero, in contrast with the second-order fluid. However, we find no contribution to the cross-stream force or migration velocity that is proportional to the second normal stress difference in the second-order fluid analyses (see Equations 3.27 and 3.69), so this difference in the constitutive equation predictions will not affect the comparison of the simulation and analytical results.

Having defined the numerical framework, we can discuss the details of the use of the FEM code for the calculation of the flow and stress fields with different boundary conditions. For the case of the freely suspended particle that is not moving in the cross-streamwise direction because the migration force is balanced by a body force, we use periodic boundary conditions on the two boundaries per-

Table 3.1: Parameters for FEM simulations

Parameter	Typical Value	Range
De	–	0.00171–0.288
$\beta = \frac{\eta_s}{\eta_0}$	0.85	0.25–0.95
λ	0.4167	0.0175–0.5
κ	0.01667	0.005667–0.3

pendicular to the streamwise direction, specifying the pressure drop over the length of the channel, and we use a constant rotation velocity boundary condition on the particle surface. In order to ensure no force on the particle in the streamwise direction, constant wall velocity boundary conditions are imposed in the direction opposite the imposed pressure gradient. An iterative process, employing the Newton-Raphson method with the rotation velocity of the particle and the wall velocity as variables, is used to determine the conditions in which the particle is both torque-free and drag-free. The appropriate wall velocity specifies the point at which the undisturbed flow velocity is zero in the fixed frame of reference. With this Galilean transformation, the mesh does not change during the calculation which considerably simplifies the numerical implementation.

Additional FEM boundary conditions used in this study logically follow from the freely suspended particle case described above, such as the use of a zero velocity boundary condition on the surface of a fixed particle. After iterating where appropriate to find the proper boundary condition, the cross-stream force can be calculated by dotting the stress vector with the unit normal vector in the cross stream direction and then integrating this stress over the surface of the particle.

The general parameters used for the simulations are summarized in Table 3.3.2.

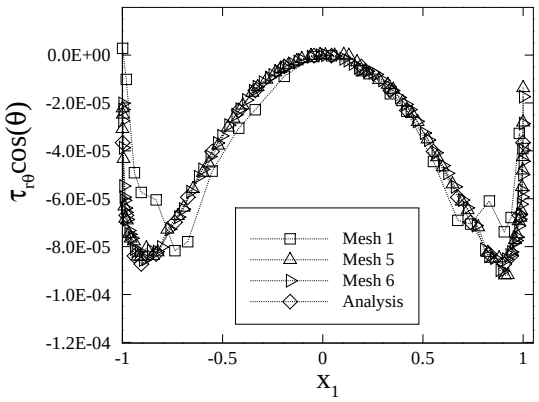

Figure 3.3: Effect of refining the FEM mesh on $\tau_{r\theta}^{(1)} \cos\theta$. Points are on the surface of the near-center half of the particle. Mesh parameters are given in Table 3.2.

For comparison with the perturbation analysis, the polymer characteristic relaxation time λ_r is set at a low value in order to make De small. The ratio of solvent viscosity to zero shear rate viscosity, β, is set to a high value in order to give only a small deviation from Newtonian behavior. λ is chosen to be near the channel center, although slightly offset in order to give a significant cross-stream force. The ratio of the particle radius to the height of the channel κ is chosen to be sufficiently small so that particle size effects do not significantly alter the bulk Poiseuille flow. Each of these variables is altered from the typical value (where the second-order fluid analysis is valid) to find how it changes the stress and velocity fields near the particle (and thus, the cross-stream force on the particle).

The mesh refinement is checked so as to ensure that there are a sufficient number of elements to accurately capture the velocity and stress fields. Figure 3.3 shows the shear stress contribution to the cross-stream force $n_2 \cdot \tau_{r\theta}$ on the near-center half of the particle based on differing meshes described in Table 3.2. Δz is the length of the smallest element near the particle in the outward normal direction (non-dimensionalized by a). The simulation parameters for these graphs

Table 3.2: Mesh refinement values.

Mesh	No. of Elements	No. of Eqs.	Δz
1	632	11201	0.25
2	1592	27681	0.019
3	2552	43089	0.009

are $\kappa = 0.0333$, $\lambda = 0.41667$, $De = 0.015$, and $\beta = 0.85$. As can be seen, the modification to the fields is almost not noticeable, except that the coarsest mesh gives a profile that does not match the analytical results very well. The level of refinement in mesh number 2 is used for all simulations, as further refining the mesh only adds computational time without changing the velocity and stress fields significantly (the x_2 force changes by 1.4% between the two refinements). The Tanner-Pipkin theorem is verified for a range of β and De, giving only minor deviations of less than 1% in the velocity field for $De < 0.2$ for all λ. The cross-stream forces on different channel lengths of the periodic cell are also checked, and the domain size used is found to be sufficiently long, giving approximately a 2% change in the predicted cross-stream force for $\kappa = 0.0167$ and a 0.02% change for $\kappa = 0.25$ for a doubling of periodic length from $L = 18$ to $L = 36$. For the fixed particle, longer meshes ($L = 480$) were used due to the larger disturbance caused by the particle. For the fixed particle case, doubling the mesh length from $L = 480$ to $L = 960$ yielded a 2% change for $\kappa = 0.0556$. A modest change (3%) in the rotation rate of the particle occurs in the simulations at $De > 0.15$ and high polymer concentration ($\beta < 0.5$), which would be expected due to the appearance of higher order De effects.

3.4 Freely suspended particle

3.4.1 Cross-stream force on a particle in Poiseuille flow

We first consider a freely suspended particle in a Poiseuille flow that has a body force that balances the cross-stream force arising due to the non-Newtonian flow, and thus does not move in the x_2 direction. We perform a parameter study in order to determine the effects of fluid properties and system geometry on the particle cross-stream force. For this system of consideration, the overall flow field must first be determined. Equation 3.1 must be solved, using a constant rotation speed boundary condition equal to the fluid rotation rate at the surface of the cylindrical particle. The wall velocity boundary conditions do not need to be specified because the linear part of the flow field decays like $1/r$ and the quadratic part decays like $1/r^2$. The Newtonian fluid velocity and pressure fields for a parallel flow are found to be—

$$\begin{aligned} u_1^{(0)} =& -\frac{4E_{21}x_1^2x_2}{r^4} + \frac{1}{2}E_{21}\left(\frac{-2x_2}{r^4} + \frac{8x_1^2x_2}{r^6}\right) + E_{21}x_2 - \Omega_{21}x_2 \\ &+ A_{122}\left(x_2^2 - \frac{1}{2} + \frac{x_1^2}{r^4} - \frac{4x_1^2x_2^2}{r^6} - \frac{1}{2r^4} + \frac{4x_1^2x_2^2}{r^8}\right), \end{aligned} \tag{3.14}$$

$$\begin{aligned} u_2^{(0)} =& -\frac{4E_{21}x_1x_2^2}{r^4} + \frac{1}{2}E_{21}\left(\frac{-2x_1}{r^4} + \frac{8x_1x_2^2}{r^6}\right) \\ &+ A_{122}\left(\frac{2x_1x_2}{r^4} - \frac{2x_1x_2}{r^6} - \frac{4x_1x_2^3}{r^8} - \frac{4x_1x_2^3}{r^6}\right), \end{aligned} \tag{3.15}$$

$$p^{(0)} = -\frac{8E_{21}x_1x_2\kappa}{r^4} - A_{122}\left(-\frac{2x_1}{r^4} + \frac{8x_1x_2^2}{r^6}\right)\kappa + 2A_{122}x_1\kappa, \tag{3.16}$$

where r is the radial coordinate, A_{ijk} is half of the second derivative of the undisturbed velocity with respect to position, $\boldsymbol{E}$ is the undisturbed rate of strain tensor, and $\boldsymbol{\Omega}$ is the undisturbed vorticity tensor, all evaluated at $x_1 = x_2 = 0$—

$$A_{122} = \frac{1}{2}\left(\frac{\partial U_1}{\partial x_2^2}\right)\Bigg|_{x_1=x_2=0}, \tag{3.17}$$

$$E_{12} = E_{21} = \frac{1}{2}\frac{\partial U_1}{\partial x_2}\bigg|_{x_1=x_2=0}, \tag{3.18}$$

$$\Omega_{21} = -\Omega 12 = \frac{1}{2}\frac{\partial U_1}{\partial x_2}\bigg|_{x_1=x_2=0}. \tag{3.19}$$

Here, U is the undisturbed velocity field. It should be noted that the particle translates with a different velocity than the imposed flow, as described by Faxén's law:

$$U_1 = \left(1 - \frac{1}{4}\frac{\partial^2}{\partial x_2^2}\right) u_1\bigg|_{x_1=x_2=0} \tag{3.20}$$

Subtracting the difference in velocity between the particle and the imposed flow, at an infinite distance from the particle ($r \to \infty$), Equations 3.14 and 3.15 yields the correct equation for a general 2D unbounded quadratic flow in the x_1 direction—

$$U_1 = A_{122}\left(x_2^2 - \frac{1}{2}\right) + E_{12}x_2 + \Omega_{12}x_2, \tag{3.21}$$

$$U_2 = 0. \tag{3.22}$$

With the Newtonian solution to the velocity field, we can apply the Tanner-Pipkin theorem in order to find the non-Newtonian velocity field. This theorem states that the O(De) contribution to the second-order fluid velocity $\boldsymbol{u}^{(1)}$ is zero and thus the velocity field equal to the Newtonian or leading order velocity solution. This is a significant departure from the second-order fluid 3D analysis of Ho & Leal [6], where the Tanner-Pipkin theorem is not applicable and the reciprocal theorem is required in order to find the particle velocity without needing to find the fluid velocity field.

To gain more physical understanding of the stresses acting on the particle, we can also write the velocity field in cylindrical coordinates r and θ and expand the θ component of velocity about $y = 0$, defined as $y = r - 1$. In this coordinate system, the velocity field consists of a simple shear flow and a solid body rotation

due to the rotation of the particle. The two parts of the velocity field can be found handily by expanding Equations 3.14 and 3.15 about $y = 0$ to yield

$$u_\theta^{SS} = 4y(E_{12}\cos(2\theta) + A_{122}\sin(\theta)\cos(2\theta)), \tag{3.23a}$$

$$u_\theta^{SBR} = -\Omega_{12} r, \tag{3.23b}$$

where the the SS superscript represents the component due to shear stress, and the SBR superscript represents the component due to solid body rotation.

With the velocity and pressure fields from the Equations 3.23 and 3.16, the different components of the cross-stream force can be determined by calculating force contributions from the the constitutive equation (Equation 3.2) and the Tanner-Pipkin pressure (Equation 3.10). It is found that the largest force contribution comes from the non-Newtonian pressure—

$$\begin{aligned} -\int_0^{2\pi} \kappa\left[-\frac{De}{\kappa}\,\boldsymbol{u}^{SBR}\cdot\nabla p^{(0)} + \left(1+4\frac{\psi_2}{\psi_1}\right) De\,\boldsymbol{e}^{SS}:\boldsymbol{e}^{SS}\right] sin\theta \;\; d\theta \\ =(-6-32\frac{\psi_2}{\psi_1}) De\,\kappa\pi E_{12}A_{122}. \end{aligned} \tag{3.24}$$

The solid body particle rotation stretching the nearby polymers also gives a cross-stream force contribution toward the center of the channel—

$$\begin{aligned} \int_0^{2\pi} \kappa\boldsymbol{n}\cdot\left[-2De(\boldsymbol{u}^{SBR}\cdot\nabla\boldsymbol{e}^{SS} - \boldsymbol{e}^{SS}\cdot\boldsymbol{\omega}^{SBR} + \boldsymbol{\omega}^{SBR}\cdot\boldsymbol{e}^{SS})\right]\cdot\boldsymbol{e_2} \;\; d\theta \\ = -\,2De\,\kappa\pi E_{12}A_{122}. \end{aligned} \tag{3.25}$$

The normal stresses due to the polymer extension in shear flow only give a cross-stream force contribution that is proportional to the second normal stress difference, which cancels the contribution proportional to the second normal stress

difference arising from the pressure exactly—

$$\int_0^{2\pi} \kappa \boldsymbol{n} \cdot \Big[-De(-4\boldsymbol{e}^{SS} \cdot \boldsymbol{e}^{SS} - 2\boldsymbol{e}^{SS} \cdot \boldsymbol{\omega}^{SS} + 2\boldsymbol{\omega}^{SS} \cdot \boldsymbol{e}^{SS}) + 8\frac{\psi_2}{\psi_1} De\, \boldsymbol{e}^{SS} \cdot \boldsymbol{e}^{SS} \Big] \cdot \boldsymbol{e_2}\ d\theta = 32\frac{\psi_2}{\psi_1} De\, \kappa\pi E_{12} A_{122}. \tag{3.26}$$

Summing the individual contributions to the cross-stream force, we obtain the overall result—

$$F_2 = 128\pi\kappa^2 De \left(\frac{1}{2} - \lambda\right). \tag{3.27}$$

Here, $E_{12} = 4\,(1/2 - \lambda)$ and $A_{122} = -4\kappa$ are substituted into the final result in order to write the cross-stream force in terms of the non-dimensional flow geometry parameters. Equation 3.27 shows that the direction of the cross-stream force is toward the center for all particle x_2 positions. The force comes entirely from the non-Newtonian components of the stress and pressure, and thus at $De = 0$, there is no force, consistent with Stokes flow reversibility.

Components of cross-stream force

A detailed look at the dominant contributions to the cross-stream force gives a physical understanding of the physical interactions of the particle and the polymeric fluid. Figures 3.4(a), 3.4(b), and 3.4(c) elucidate the mechanism of migration in the second-order fluid limit, showing the analytical predictions for the migration force integral contributions for a particle at $\lambda = 0.41667$, $\kappa = 0.0167$, and $De = 0.00863$.

From the analysis, we find that the cross-stream force is not proportional to the second normal stress difference coefficient. Considering terms not proportional

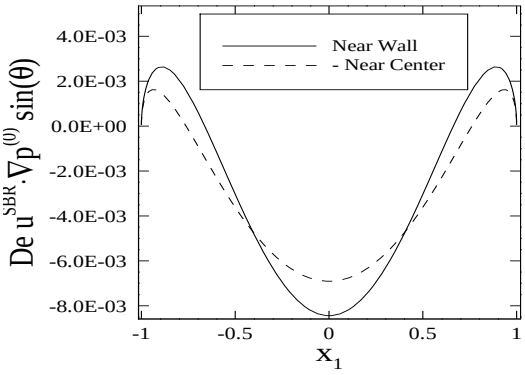

(a) Parts of pressure contribution to F_2: $\boldsymbol{u^{SBR}} \cdot \nabla p^{(0)}$.

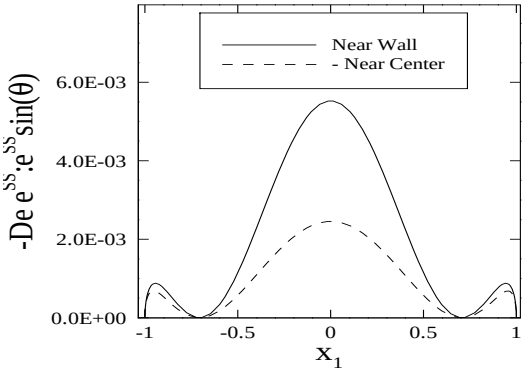

(b) Parts of pressure contribution to F_2: $\boldsymbol{e^{SS}} : \boldsymbol{e^{SS}}$.

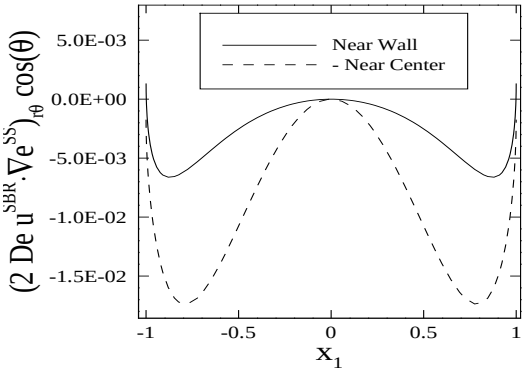

(c) Parts of $\tau_{r\theta}$ contribution to F_2: $\boldsymbol{u^{SBR}} \cdot \nabla \boldsymbol{e^{SS}}$.

Figure 3.4: Contributions to the non-Newtonian part of the analytical expression for overall stress on the particle surface. $\kappa = 0.0167$, $De = 0.00863$, $\lambda = 0.416667$.

to ψ_2, we find that contributions to the cross-stream force arise from the pressure (75% of the total contribution) and the $r\theta$ component of the stress (25% of the total contribution). The integrals of the rr and $\theta\theta$ components of the stress are zero, and thus these components of the stress are non-contributing. The pressure contribution arises because the non-Newtonian pressure on the near-wall side of the particle is significantly higher than that on the near-center side, due to a higher shear rate on the near-wall side, as described below. In Figures 3.4(a) and 3.4(b), the first and second terms of Equation 3.24, respectively, are plotted. The first term is the convection of the Newtonian pressure, and the second term is the deformation of the fluid due to the shear stress around the particle. The convective pressure term actually gives a contribution to F_2 toward the wall, arising due to the larger pressure gradient on the near wall side of the cylinder. However, the total contribution to the force due to the pressure is principally derived from the difference in the deformation of the polymer at the near-wall surface of the particle and the near-center surface of the particle (shown in Figure 3.4(b)), with a contribution four times larger than the convection of pressure term. A second contribution to the force comes from the shear stress $\tau_{r\theta}$; as shown in Figure 3.4(c), the $\tau_{r\theta}$ contribution arising from the convection of $\boldsymbol{e}$ points toward the center of the channel. The $\tau_{r\theta}$ contribution arises mainly from the differences in the near-center shear stress peaks at $\theta = \pi/4$ and $\theta = 3\pi/4$ and the near-wall shear stress peaks at $\theta = 5\pi/4$ and $\theta = 7\pi/4$ of the particle, which are larger in magnitude on the near-wall half of the particle than on the near-center half of the particle.

Thus, in total, the non-Newtonian contributions to the cross-stream force toward the center come from the convection of $\boldsymbol{e}$ and the deformation of the fluid ($\boldsymbol{e} : \boldsymbol{e}$), while the convection of the Newtonian pressure provides a contribution toward the wall.

Related to this discussion, an explanation proposed by Ho and Leal [6] for this difference in stress is related to the so-called hoop stress on the particle surface. In inhomogeneous shear flows, polymers will stretch different amounts depending on the local shear rate. The polymer strands have greater extensions at higher shear rates; hence, they will provide a greater normal stress on the particle, and the particle will move toward the direction of the lower shear rate.

Comparison of analytical and FEM results

In the limits of slow flow ($De \ll 1$), small particle size ($\kappa \ll 1$), and particle location far enough from the wall ($\lambda \gg \kappa$ and $1 - \lambda \gg \kappa$), the analytical and simulation results converge. This can be seen in Figure 3.5, which is for $\lambda = 0.41667$, $De = 0.00863$, and $\kappa = 0.0167$. The curves on the near-center side of the particle are multiplied by -1 to aid in comparison. The particle coordinate position x_1 varies from $x_1 = -1$ to $x_1 = 1$ and increases in the direction of $\boldsymbol{U}$. The analytical points are determined by substituting the Newtonian velocity and pressure fields (Equations 3.14, 3.15 and 3.16) into the second-order fluid stress and pressure (Equations 3.2 and 3.10, respectively). The FEM points for the velocity gradient and the non-Newtonian shear stress are obtained directly from the simulation output. However, the pressure is output as a combined Newtonian and non-Newtonian pressure, and thus the non-Newtonian pressure must be determined in a different manner. We assume that at low De, the pressure scales with De based on the expression for the second-order fluid pressure (Equation 3.10). Thus, we perform a second simulation at $De = 0.00877$ and combined that with the first simulation to find the non-Newtonian pressure—

$$p^{(1)} = \frac{p_{sim2} - p_{sim1}}{De_{sim2} - De_{sim1}}, \tag{3.28}$$

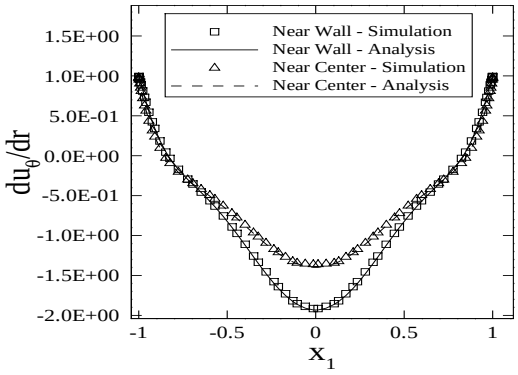

(a) du_θ/dr.

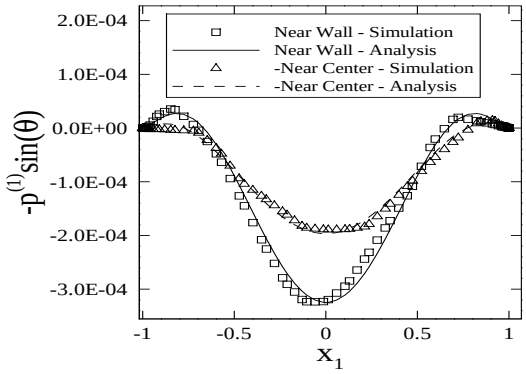

(b) $\text{-}p^{(1)} \sin\theta$.

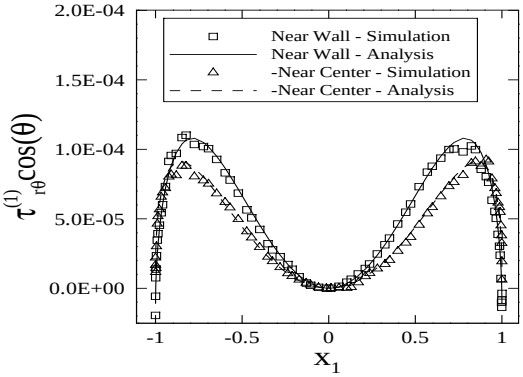

(c) $\tau_{r\theta}^{(1)} \cos\theta$.

Figure 3.5: Comparison of the velocity gradient, pressure, and shear stress on the surface of a freely suspended particle. $\lambda = 0.41667$, $\kappa = 0.0167$, $De = 0.00863$, $\beta = 0.85$.

As the comparison shows, the stress, pressure, and velocity gradient fields from the analytical predictions and the simulation results have very good agreement.

We can also use Figure 3.5 to analyze the contributions to the cross-stream force in terms of the flow field properties rather than the individual terms in the force integrals, as was done in Section 3.4.1. First, from Figure 3.5(a), there is an imbalance of shear stress on the near-wall and near-center sides of the particle, causing an increased pressure (Figure 3.5(b)). The shear stress (3.5(c)) contribution arises from near the sides of the particle, pointing toward the center of the channel. The rr component of the stress is not shown, as it is zero. The only contributions to the force come from the non-Newtonian pressure and the $r\theta$ component of the $\boldsymbol{u} \cdot \nabla \boldsymbol{e}$ term.

Streamlines for the flow around the cylinder are presented in Figure 3.6, showing a section of closed streamlines near the cylinder and a section of open streamlines farther away from the cylinder. The velocity field for this zero Re, finite De case exhibits two stagnation points and wakes with reversing trajectories. In order to understand this flow field, it is helpful to review past studies that have examined the streamlines around a cylinder in shear flow. For an unbounded Newtonian shear flow at $Re = 0$, for both a cylinder and a sphere, there is a region of open streamlines and a region of closed streamlines that extends to $x_1 \rightarrow \pm\infty$ with no saddle point [16]. Two different flow cases where a saddle point has appeared have been previously identified—1) for a Newtonian flow past a cylinder at finite Re [13], and 2) for a Newtonian flow past a sphere at $Re = 0$ in a bounded domain [19]. We do not observe saddle points for the Newtonian flow for $\kappa = 0.01667$, due to large size of the domain relative to the particle size; thus, the saddle points only arise at finite De. Subramanian & Koch [17] showed that the fluid velocity field is qualitatively similar for small De and small Re flows near a freely suspended

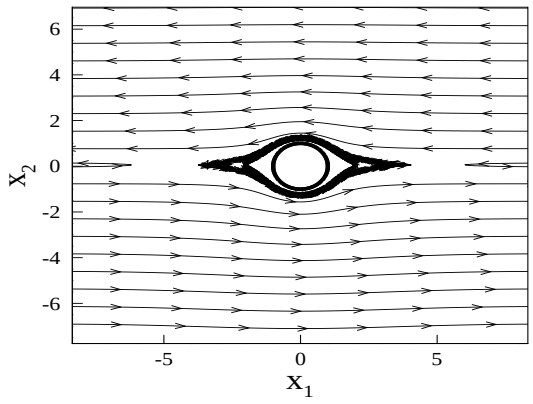

Figure 3.6: Streamlines near freely suspended particle. $De = 0.288$, $\lambda = 0.41667$, $\kappa = 0.01667$, $\beta = 0.25$.

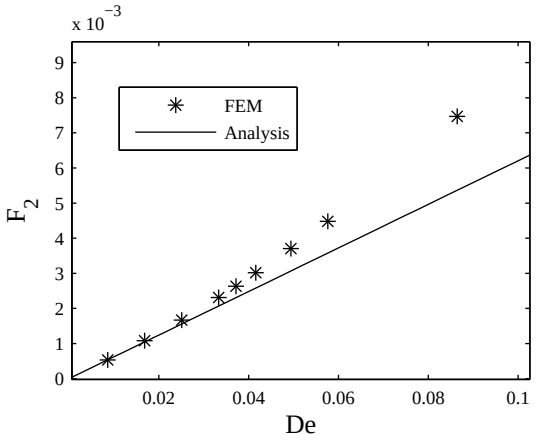

Figure 3.7: Cross-stream force dependence on De for a freely suspended particle. $\lambda = 0.41667$, $\kappa = 0.0167$, $\beta = 0.85$.

sphere in shear flow; based on this result along with Robertson & Acrivos's [13] finding for a cylinder, the presence of saddle points in the finite De cylinder case would be expected.

De effect

FEM simulations are used to extend the O(De) analytical results to higher De by changing the relaxation time of the fluid (and thus from an experimental point of view, the choice of polymer). The simulation results show O(De^2) effects; the simulation points can be fitted to a quadratic curve $F_2 = 0.00135De + 0.00104De^2$. The linear term matches very well with the analytical prediction of $F = 0.00139$. A finite relaxation time shifts the stress peaks in the direction of the fluid rotation, causing a departure from the predicted linear scaling. The pressure term is the main source of this deviation, with a contribution three times larger than that from the shear stress term.

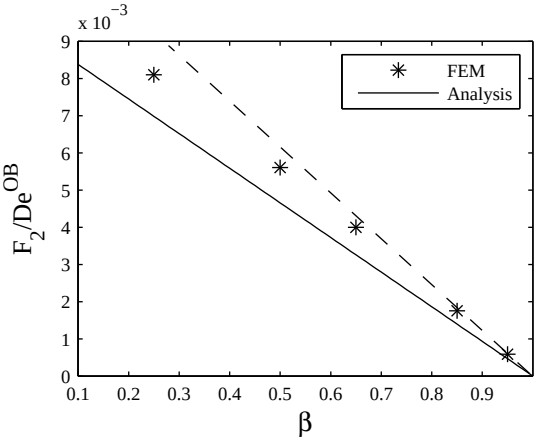

Figure 3.8: Cross-stream force dependence on the ratio of solvent viscosity to zero shear rate viscosity (β) for a freely suspended particle. $De^{OB} = 0.384$, $\lambda = 0.41667$, $\kappa = 0.01667$.

Polymer concentration effect

The contribution by the polymer to the solution viscosity is given by $1 - \beta$, where β is defined as the ratio of the solvent viscosity to the zero shear rate viscosity. Simulations at several values of β are carried out, and the results are shown in

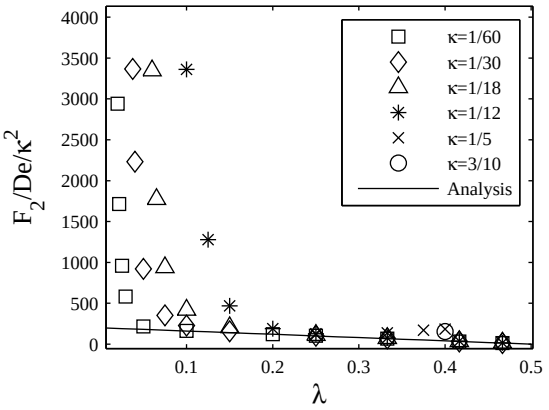

Figure 3.9: Cross-stream force dependence on particle size and cross-stream position for a freely suspended particle. $\beta = 0.85$.

Figure 3.8. In the figure, De^{OB} is kept constant, which physically is the same as varying the polymer concentration of a high molecular weight polymer in a solvent (Boger fluid) while keeping its relaxation time constant. For the limit of $1-\beta \ll 1$, the velocity field is unaltered by the polymer for all De because the dilute polymers in solution do not interact. As long as the velocity field is the same, there should still be a linear scaling of $1-\beta$ with De. Thus, the non-Newtonian stresses are proportional to $1-\beta$ for all De; however, the slope of this line changes with De due to the finite relaxation time of the polymers, which affects the cross-stream force scaling with De, as seen in Section 3.4.1. Due to the high De^{OB} of 0.384 used in this comparison study, a significant deviation due to finite De is shown by the included dashed line, which is formed from the first point and the limit of zero polymer concentration. A second deviation occurs due to the change in the velocity field at lower β, where higher polymer concentration causes the flow and stress fields to change. As Figure 3.8 shows, the cross-stream forces at lower β values deviate from the predicted linear scaling given by the dashed line.

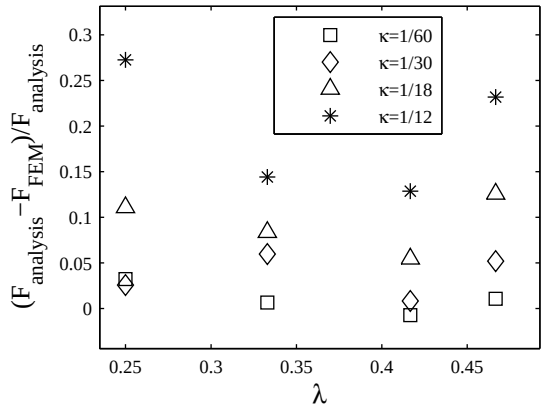

Figure 3.10: Deviation from analytical prediction far from the wall due to particle size for a freely suspended particle. $\beta = 0.85$.

Particle-wall hydrodynamic interactions

Particles close to the wall and particles that are large are studied with FEM simulations, since the theory requires that the particle disturbance to the velocity and stress fields decay rapidly and thus, that the reflection of the disturbance off of the wall be negligible. As can be seen in Figure 3.9, the analysis gives accurate predictions for a wide range of particle positions and sizes, but near the wall, the force on the particle increases dramatically. Points in Figure 3.10 show that for a large particle size, there is also a deviation from analytical prediction for the cross-stream force, although the deviation is small compared to the large forces on the particles near the wall. For the largest size particles that is simulated ($\kappa \geq 0.2$), the simulations for particles positioned near the wall do not converge, and thus only the points where the particle is nearer to the channel center are shown.

A requirement of the analysis outlined in Section 3.4.1 is that the particle radius be much smaller than the distance of the particle to the nearest wall. This condition is allowed in the system of consideration because for most particle locations, the

force on the particle due to the shear rate gradient in the undisturbed Poiseuille flow is much greater than the force due to the reflection of the particle disturbance to the velocity, pressure, and stress fields off the wall. This is in contrast to a linear flow, where the shear rate in the undisturbed flow is uniform and hence does not provide a driving force for migration, so the reflections of the disturbance to the flow field by the cylinder must be included in order to obtain a net migration force [6]. However, near the wall in a Poiseuille flow, the reflection of the flow field disturbance off the walls due to the particle becomes larger than the force due to the shear. In this region, the particle rotates at a slower rate than predicted by theory, and the surface velocity gradient is noticeably higher on the near-wall side of the particle, indicating that the disturbance that the particle creates in the flow field does not decay completely. Accompanying changes in the shear stress and non-Newtonian pressure fields on the near wall side of the particle surface occur, resulting in a larger cross-stream force than predicted.

Larger particle sizes magnify the changes in the flow fields due to a particle's proximity to the wall, causing even larger deviations from the analysis. It should also be noted that due to the larger size of the particle, the values of the undisturbed rate of strain tensor on the near-wall and near-center sides of the particle are not the sufficiently close to the value of the undisturbed rate of strain tensor at the λ value for the center of the particle, as is assumed in the analysis. These factors lead to a net cross-stream force on the larger particle that is higher than that predicted by the analysis. There is also an increase in the deviation from the analysis for larger particles near the center of the channel. For large particles near the center line, the particle crosses over the channel centerline, and the velocity gradient is no longer in the same direction on the near-wall and near-center sides of the particle. At very larger particle sizes ($\kappa \geq 0.2$), the deviations in the lift

force continue to grow. Due to the difficulty of convergence, only a few points are shown, but all simulations show cross-stream forces on the particle pointing toward the channel center. These results contrast with the simulation results of Huang et. al [7], who found that cylindrical particles experienced a migration force in Poiseuille flow that pointed toward the channel wall for a large particle of size $\kappa = 0.25$. The current study, on the other hand, finds no switch in the particle migration direction. Possible reasons for the discrepancy are discussed in Section 3.5.2.

Lubrication interactions

Nearer to the wall, particles in the lubrication regime experience a very high cross-stream force pointing toward the center of the channel. In this section, the reasons for this large force will be discussed, and an analytical solution for the lubrication regime will be developed. In order to account for interactions of the particle very near to the wall, we perform a separate analysis that is valid in the lubrication regime. Previous investigators determined the velocity, pressure, and stress fields for a lubricating particle. The resultant force and torque due to lubrication will be summed with a second force and torque derived from a shear flow on a stationary particle and set to zero in order to obtain the correct force-free, torque-free particle boundary condition. These equations will give us the particle rotation speed and translation velocity, which we will compare to simulation data. We will also find the second-order fluid lubrication force by applying the Tanner-Pipkin theorem to determine the non-Newtonian flow field and then integrating Equations 3.2 and 3.10 on the surface of the particle,

Jeffrey and Onishi [9], who studied the motion of a cylinder near a wall sus-

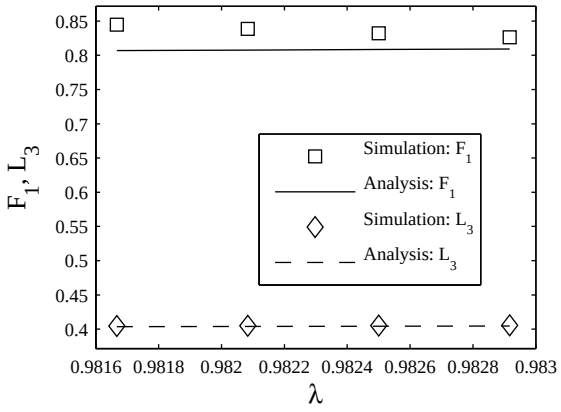

Figure 3.11: Comparison of the magnitude of the force and torque on a stationary particle near the wall due to Newtonian Poiseuille flow. $\kappa = 0.01667$.

pended in a Newtonian fluid, examined the lubrication regime by extending their results to the limit of small gap thickness and found the following expressions for the velocity and pressure fields for a rotating, translating cylinder—

$$u_1^{lub} = \left(-\frac{1}{h^2} + \frac{2X_1^2}{h^3} \right) X_2(X_2 - h)(\omega - v_1) + \frac{X_2}{h}(\omega + v_1), \tag{3.29}$$

$$p^{lub} = \frac{2X_1}{h^2 \epsilon^{1/2}}(\omega + v_1). \tag{3.30}$$

where ϵ is the non-dimensional gap distance between the particle and the wall, $X_1 = x_1/\epsilon^{1/2}$ and $X_2 = (x_2 + d)/\epsilon$ are stretched coordinates, h is the value of the X_2 coordinate at the cylinder surface and is equal to $h = 1 + X_1^2/2$, ω is the particle rotational speed, and v_1 is the particle translational velocity.

They found the lubrication force and torque to be–

$$F_1^{lub} = \frac{-4\pi v_1 \kappa}{\sqrt{2\epsilon}}, \tag{3.31}$$

$$L_3^{lub} = \frac{-4\pi \omega \kappa}{\sqrt{2\epsilon}}. \tag{3.32}$$

Jeffrey and Onishi's solution method can also be used to find the force and torque on a stationary particle near the wall ($\epsilon << 1$) for a velocity field that

approaches a linear shear flow far from the particle. First, the general solution $\nabla\psi^4 = 0$ (where ψ is the stream function) for a Stokes flow field in bipolar coordinates is expressed as an infinite sum. The gap is assumed to be very small, allowing appropriate approximations for trigonometric functions in the velocity expression. Then, the disturbance velocity is set equal to the particle velocity minus the velocity due to the shear flow. This yields an expression that can be solved to find the velocity and pressure fields around the cylinder. With the appropriate coefficients determined for the velocity field, the drag force and torque on a stationary particle in a shear flow are found—

$$F_1^{stationary} = 8\pi\gamma\kappa, \tag{3.33}$$

$$L_1^{stationary} = -4\pi\gamma\kappa, \tag{3.34}$$

where γ is the non-dimensional shear rate and is equal to two for a Poiseuille flow.

We compare the results from Equations 3.33 and 3.34 to simulation results where the particle is held fixed in a Poiseuille flow. Results in Figure 3.4.1 show good agreement for the force and torque on a stationary particle in the lubrication regime. Since there is no net force or torque on the particle, the lubrication force and torque exactly cancel the force and torque from the shear flow, and from this relationship, the particle translation and rotation velocities can be found.

Setting the sums of Equations 3.31 and 3.33, and Equations 3.32 and 3.34, respectively, equal to zero, we find the translation and rotation velocities to be—

$$v_1 = 4\sqrt{2\epsilon}, \tag{3.35}$$

$$\omega = -2\sqrt{2\epsilon}. \tag{3.36}$$

Equations 3.35 and 3.36 are compared with simulation results in Figure 3.12, again showing agreement. Thus, all of the Newtonian analytical results are verified by FEM results.

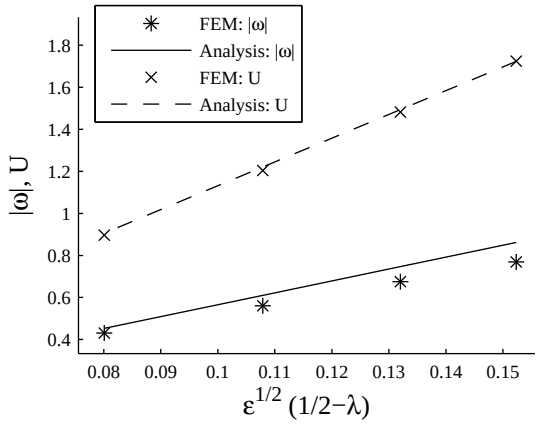

Figure 3.12: Comparison of translation velocity and rotation speed of a lubricating particle in a Newtonian Poiseuille flow. $\kappa = 0.01667$.

Next, in the same manner as the freely suspended particle analysis, we invoke the Tanner-Pipkin theorem in order to use the Newtonian velocity field from Jeffrey and Onishi's analysis as the second-order fluid velocity field. The non-Newtonian pressure field, as before, is given by Equation 3.10. The cross-stream force on the particle is then found by integrating the stress (Equation 3.2) over the surface of the particle to find—

$$F_{2,lub} = \frac{3\pi\sqrt{2}\kappa De}{2\epsilon^{3/2}} \left[\omega^2 + v_1^2\right]. \tag{3.37}$$

Substituting Equations 3.35 and 3.36 into the result, we obtain—

$$F_{2,lub} = \frac{60\pi\sqrt{2}\kappa De}{\epsilon^{1/2}}. \tag{3.38}$$

The analytical and simulation results in the lubrication regime do not match. The non-Newtonian pressure, which is the dominant contribution to the cross-stream force, does not decay in the lubrication gap as it would be expected to. This leads the authors to believe that the smallest gap that was simulated ($\epsilon = 0.0275$ at $\kappa = 0.01667$) was not sufficiently close to the wall. At the closest point, the simulation predicted a lubrication force of 0.024 while the analysis predicted a much smaller force of 0.011. Further simulations with smaller gaps rendered the

code unstable, and thus no convergent results were obtained. Nevertheless, the analytical result provides a good prediction of the behavior of the particle as it approaches the wall, showing that the lubrication force points toward the channel center.

3.4.2 Particle migration velocity

Having performed an extensive parameter study for the case in which a particle has a hydrodynamic force from the fluid that is balanced by a body force, we now remove the body force and allow the particle to migrate in the cross stream direction. In contrast to Section 3.4.1, the O(De) hydrodynamic force is balanced now by the Newtonian viscous resistance to translation normal to the wall, which yields the correct force-free particle boundary condition. In order to find the O(De) migration velocity, a relationship between the particle translation velocity and the force that resists the translation must be determined. This expression is found by considering the case of a particle that is translating perpendicular to the wall without an imposed flow. The resultant velocity field can be superimposed with Equations 3.14 and 3.15 to obtain the overall velocity field for the case where the particle is simultaneously translating in the cross stream direction (migrating) and streamwise direction in a Poiseuille flow.

In order to understand the scaling arguments for the migration velocity, let us first consider the case of the particle that is migrating in the cross-stream direction with an imposed Poiseuille flow. Due to Stokes reversibility, there is no cross-stream force or migration velocity at O(1), and thus the force on the particle from the flow field and the particle migration velocity are written as–

$$F_2 = DeF_2^{(1)} + O(De^2), \tag{3.39}$$

$$v_2 = De v_2^{(1)} + O(De^2). \tag{3.40}$$

This cross-stream force is opposed by a Newtonian resistance force, which can be determined by considering the case of a particle that is translating perpendicular to the wall without an external flow field—

$$\bar{F}_2 = De \bar{F}_2^{(1)} + O(De^2), \tag{3.41}$$

$$\bar{v}_2 = De \bar{v}_2^{(1)} + O(De^2), \tag{3.42}$$

where the bar denotes a quantity for the case in which we consider a particle translating perpendicular to the walls. The velocity field $\bar{u}_2$ found from the Newtonian flow for a particle translating in the 2 direction creates a disturbance that drives an order De velocity field, which creates an order De force that balances the order De force that arises from the Poiseuille flow. The leading order term in the Newtonian translation problem is based on O(De) effects from the Poiseuille flow. Thus, the cross-stream force from Equation 3.27 is balanced by $\bar{F}_2$, yielding no net force on the migrating particle.

As outlined above, we must first find the relationship between the particle force and velocity on a particle translating perpendicular to the wall. In order to simplify the presentation, we do not include the superscript (1) to indicate that all of the stress and velocity field variables are $O(De)$. We start by writing the governing equations for this situation—

$$\nabla \cdot \bar{\boldsymbol{\tau}} = 0, \quad \nabla \cdot \bar{\boldsymbol{u}} = 0, \tag{3.43}$$

$$\bar{\boldsymbol{\tau}} = -\bar{p}\boldsymbol{I} + 2\bar{\boldsymbol{e}}. \tag{3.44}$$

where $\bar{\boldsymbol{e}}$ is of the same form as given by Equation 3.18. Note that the non-dimensionalization for this case is different, with a force scale of $\eta\bar{v}_2$ and a time scale of $a/\bar{v}_2$, where $\bar{v}_2$ is the particle translation velocity. In order to solve this

set of equations, the system is divided into inner and outer regions. In the inner region, the walls are not taken into account, which is valid when the radial coordinate r from the particle center is much less than $1/\kappa = H/a$. The flow field is calculated by taking a multipole expansion of the fluid velocity and pressure fields and applying a constant rotation speed boundary condition on the surface of the particle. An additional expression that relates the force of the fluid on the particle to the particle velocity is found by integrating the stress tensor on the particle surface. This expression is incorporated into the equations for the velocity and pressure fields, giving the following—

$$\begin{aligned}\bar{u}_{i,inner} =& \frac{\bar{F}_j}{4\pi}\left[\delta_{ij}\left(\ln(r) - \frac{1}{2r^2} + \frac{1}{2}\right)\right. \\ & \left. - \frac{x_i x_j}{r^2}\left(1 - \frac{1}{r^2}\right)\right] + \bar{v}_i,\end{aligned} \tag{3.45}$$

$$\bar{p}_{i,inner} = -\frac{\bar{F}_i x_i}{2\pi r^2}. \tag{3.46}$$

where $\bar{F}$ is the force of the fluid on the particle and $\bar{v}_i$ represents the translation velocity of the particle. In order to match the inner solution with the outer one, only the terms that do not decay are kept—

$$\bar{u}_{i,matching} = \frac{\bar{F}_j}{4\pi}\left[\delta_{ij}\left(\ln(r) + \frac{1}{2}\right) - \frac{x_i x_j}{r^2}\right] + \bar{v}_i. \tag{3.47}$$

Taking the Fourier transform of the spatially varying terms in Equation 3.47 with respect to x_1 and noting that $\bar{F}_i$ and $\bar{v}_i$ are only in the 2 direction gives

$$\tilde{\bar{u}}_{1,matching} = -\frac{i\bar{F}_2}{4}\,\mathrm{sgn}(k_1) x_2 e^{-2\pi|k_1||x_2|}, \tag{3.48}$$

$$\tilde{\bar{u}}_{2,matching} = \frac{\bar{F}_2}{4\pi}\left[\frac{-1}{2|k_1|} - \pi|x_2|\right] e^{-2\pi|k_1||x_2|}, \tag{3.49}$$

where the tilde above the variables indicates a Fourier transform in the x_1 direction. Now turning to the outer region, a system at a distance $r >> 1$ is considered. For

this region, we use H as the length scale and $H/\bar{v_2}$ as the time scale. To find the solution in the outer region, the Stokes and continuity equations (Equations 3.43 and 3.44) are solved using Fourier transforms, assuming that the particle is a point force and using a zero velocity boundary condition at the walls. Writing Equations 3.43 and 3.44 in Fourier space gives

$$-(2\pi k_1)^2 \tilde{\tilde{u}}_{i,outer} + \frac{d^2 \tilde{\tilde{u}}_{i,outer}}{dx_2^{\S 2}} = \delta_{i1} 2\pi i k_1 \tilde{\tilde{p}}_{outer} + \delta_{i2} \frac{d\tilde{\tilde{p}}_{outer}}{dx_2^{\S}}, \qquad x_2^{\S} \neq 0 \tag{3.50}$$

where the § superscript indicates an outer solution position. Using the fact that for a creeping flow, the laplacian of the pressure is zero, we find—

$$\tilde{p} = Ae^{-2\pi|k_1|x_2} + Be^{2\pi|k_1|x_2} \tag{3.51}$$

The solution to Equation 3.50 is then—

$$\tilde{\tilde{u}}_{1,outer} = \left(C_1 - Ai\,\mathrm{sgn}(k_1)x_2^{\S}\right) e^{-2\pi|k_1|x_2^{\S}} + \left(D_1 + Bi\,\mathrm{sgn}(k_1)x_2^{\S}\right) e^{2\pi|k_1|x_2^{\S}}, \tag{3.52}$$

$$\tilde{\tilde{u}}_{2,outer} = \left(C_2 - Ax_2^{\S}\right) e^{-2\pi|k_1|x_2^{\S}} + \left(D_2 + Bx_2^{\S}\right) e^{2\pi|k_1|x_2^{\S}}. \tag{3.53}$$

It should be noted that Equations 3.52–3.53 have the same form for both $x_2^{\S} < 0$ and $x_2^{\S} > 0$, although the coefficients are different, depending on the sign of $x_2^{\S}$. For example, C_i for a positive $x_2^{\S}$ would be D_i for a negative $x_2^{\S}$.

Based on the force terms in the inner solution, some of the coefficients in the Equations 3.52 and 3.53 should have Heaviside step functions ($\mathrm{H}(x_2^{\S})$) associated with them, and thus new coefficients are defined as follows—

$$\begin{aligned}
A &= A' - \frac{\bar{F}_2}{4}\,\mathrm{H}(x_2^{\S}), \\
B &= B' - \frac{\bar{F}_2}{4}\left[\mathrm{H}(x_2^{\S}) - 1\right], \\
C_2 &= C_2' - \frac{\bar{F}_2}{8\pi|k_1|}\,\mathrm{H}(x_2^{\S}), \\
D_2 &= D_2' - \frac{\bar{F}_2}{8\pi|k_1|}\left[1 - \mathrm{H}(x_2^{\S})\right].
\end{aligned} \tag{3.54}$$

The primed coefficients (A', B', C_2', and D_2') are continuous at $x_2^{\S} = 0$ whereas the unprimed coefficients (A, B, C_2, and D_2) are discontinuous at $x_2^{\S} = 0$.

Next, we apply zero velocity boundary conditions at the walls and mass conservation to obtain six equations for the six unknowns. After lengthy algebraic manipulations, the expressions for all of the coefficients are obtained. With these coefficients, we then take Equation 3.53 and set $x_2^{\S} = 0$ in order to match the solutions near the particle. The outer solution velocity field is found to be—

$$\bar{u}_{2,outer}(x_2^{\S} = 0) = -2\pi \int_{-\infty}^{\infty} \left[C_2' + D_2' + \frac{1}{2\pi|k_1|} \right] e^{2\pi i k_1 x_1^{\S}} \; dk_1. \tag{3.55}$$

After this step, the inner and outer solutions for the translating particle system are matched by setting the inner solution fluid velocity field as $x_1 \to \infty$ equal to the outer solution fluid velocity field as $x_1^{\S} \to 0$:

$$\lim_{x_1 \to \infty} \frac{\ln|x_1|}{\pi} + \frac{4\bar{v}_2}{\bar{F}_2} + \frac{1}{2\pi} - \frac{\ln\left(\frac{1}{\kappa}\right)}{\pi} = - \lim_{x_1^{\S} \to 0} \int_{-\infty}^{\infty} \left[C_2' + D_2' + \frac{1}{2\pi|k_1|} \right] e^{2\pi i k_1 x_1^{\S}} \; dk_1. \tag{3.56}$$

This step is valid because both solutions apply in the region where the coordinate r is such that $1 \ll r \ll 1/\kappa$. As the limits on the left and right hand sides of the equation are approached, the expressions become singular. In order to write the equation in a form such that it is continuous, we find a quantity c that we know the Fourier transform of and that decays as $q \to \infty$ with $1/q$ and approaches a constant as $q \to 0$. This is in order to ensure no singularities in the integral derived from the outer solution. We determine the constant to be—

$$c = -\frac{1}{2} Y_0(\sqrt{\zeta} r). \tag{3.57}$$

where Y_0 is a Bessel function. Taking the Fourier transform of Equation 3.57, we obtain

$$\hat{c} = -\frac{1}{\sqrt{4\pi^2 k_1^2 + \zeta}}. \tag{3.58}$$

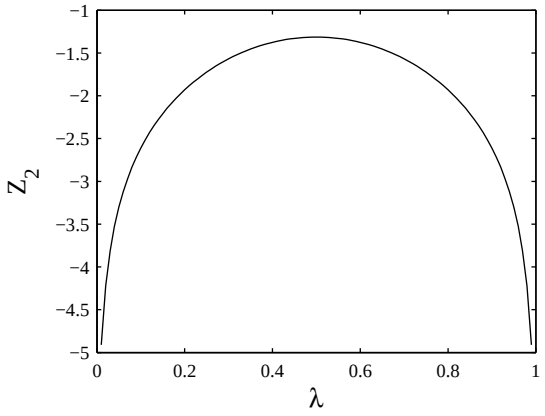

Figure 3.13: Dependence of Z_2 on particle position in the channel.

Adding the quantities from Equations 3.57 and 3.58 to the left and right sides, respectively, of Equation 3.56 yields the end result for the particle translation velocity—

$$\bar{v}_2 = -\frac{\bar{F}_2}{4\pi}\left[\ln\left(\frac{1}{\kappa}\right) + Z_2\right]. \tag{3.59}$$

where Z_2 is a function of λ that arises from the Fourier transforms—

$$\begin{aligned} Z_2 =& 0.616 - \frac{1}{2}\lim_{\zeta>>1}\ln(\zeta) \\ &+ 2\pi\int_0^\infty \lim_{\zeta>>1}\left[C_2' + D_2' - \frac{1}{2\pi k_1} + \frac{1}{\sqrt{4\pi^2 k_1^2 + \zeta}}\right]\, dk_1. \end{aligned} \tag{3.60}$$

In this equation, ζ is a constant that must be much smaller than $2\pi k_1$ and much larger than $1/\lambda^2$. C_2' and D_2' are functions of λ, but the expressions are too lengthy to reproduce here. Figure 3.13 shows the dependence of Z_2 on x_2.

FEM simulations are used to verify the validity of Equation 3.59. The domain is made very large ($1/\kappa = 100$) in order to satisfy the small particle limit of the theory. A constant fluid velocity boundary condition is specified in the x_2 direction on the cylinder surface, and the wall velocity boundary conditions are set to zero. The cylinder is fixed in place, and the force on the particle due to the fluid motion

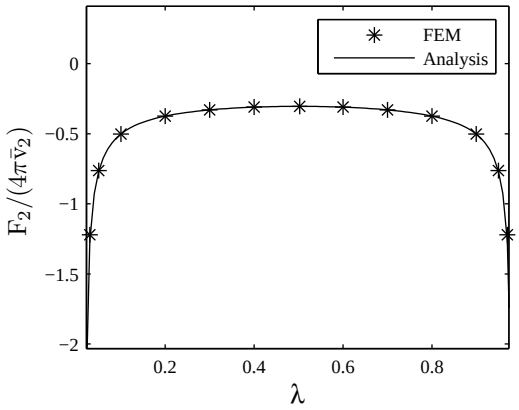

Figure 3.14: Comparison of translation force for particle motion perpendicular to the channel wall. κ=0.01.

near the surface of the particle is calculated. This implementation is valid as a result of the quasi-steady nature of Stokes Newtonian flow, where the fluid velocity and pressure only depend on the instantaneous position and velocity of the particle.

The comparison to simulations is performed by matching the particle velocity from Equation 3.59 to the value of the particle velocity used in the simulation. Figure 3.14 shows good agreement for all values of λ, validating the analytical expression. The force that opposes particle migration increases dramatically at the walls and has a minimum at the middle of the channel.

With Equations 3.27 and 3.59, the particle migration velocity can be found by summing the cross-stream force contributions from the problem of the torque-free, no streamwise force particle in Poiseiulle flow and the problem of the translating particle and setting them to zero, so that there is the correct no net force boundary condition on the particle. The result for the dimensional migration velocity is as follows—

$$v_2^* = 32\kappa^3 U_{max} De \left(\frac{1}{2} - \lambda\right)\left(\ln\left(\frac{1}{\kappa}\right) + Z_2\right). \tag{3.61}$$

With this expression for the migration velocity, the effects of the fluid properties,

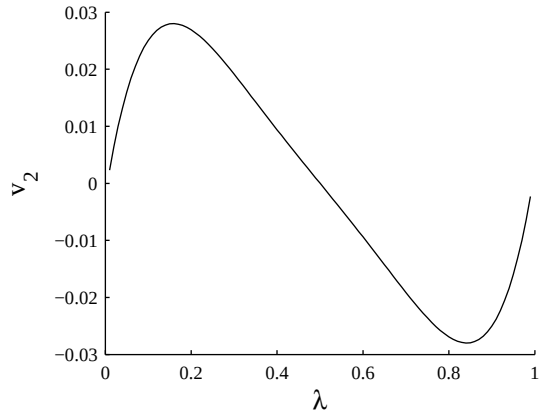

Figure 3.15: Dependence of freely suspended particle migration velocity on channel position. The plot is antisymmetric about the centerline, where there is no migration. v_2 is non-dimensionalized by $U_{max}\kappa$. $De = 0.1$, $\kappa = 0.01$.

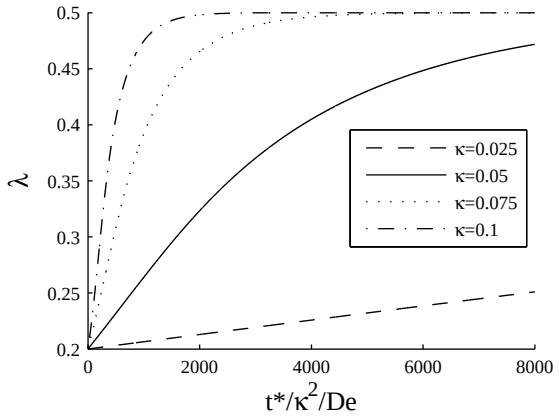

Figure 3.16: 2D freely suspended particle trajectories for different κ values. t is non-dimensionalized by H/U_{max}.

the distance from the wall, and the particle size on the migration velocity can be determined. Migration velocity as a function of vertical position is plotted in Figure 3.15.

Figure 3.16 shows the non-dimensional plot of the particle migration dependence on the particle size, showing that even when scaling out the κ dependence, the $\ln(\kappa)$ term is an important factor. The trajectory plot is made by first finding

the velocity of the particle based on the fluid position and then multiplying the fluid velocity by a sufficiently small time step δt, assuming constant particle and fluid velocity over that time. After each step, a new λ value is calculated and the next change in position is determined. In this method, the time derivatives are ignored, and therefore transient effects due to the particle migration are assumed to be minimal.

Comparison of migration velocity of cylinders and spheres at low De

The 2D result shares many of the same features with the 3D solution found by Ho & Leal [6], rewritten here in the notation used in this paper:

$$v^*_{2,3D} = \frac{160}{9}\kappa^2 De\left(\frac{1}{2}-\lambda\right)\left(1-2\frac{\psi_2}{\psi_1}\right). \tag{3.62}$$

However, there are some key differences that should be noted. First, in three dimensions, the velocity has an additional term that is proportional to the ratio of the second to first normal stress difference coefficients. Since most fluids have a positive first normal stress difference and a negative second normal stress difference, the migration velocity should be enhanced due to this additional term. In contrast, there is no second normal stress difference effect in the 2D case. Secondly, in the 2D case, due to the particle-wall hydrodynamic interaction (Figure 3.14), the drag force on the particle is very high and migration velocity is very small for particles close to the wall; the 3D case does not have this effect due to the fact that the walls do not affect the drag on the particle, as given by Stokes's drag law. Lastly, the dependence on κ is different in the two geometries: the velocity of the cylinder is proportional to κ^3, while the velocity of the sphere is proportional to κ^2. This is to be expected because the Newtonian drag on the cylinder is a factor of κ larger than the Stokes drag on a sphere, so the sphere migrates at a faster velocity.

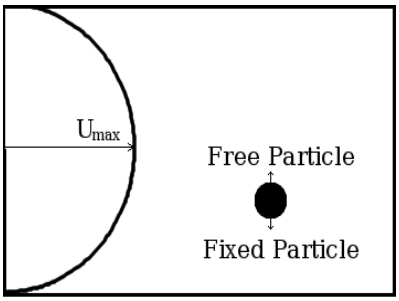

Figure 3.17: Direction of cross-stream force for different boundary conditions.

3.5 Fixed particle

We now turn our attention to a fixed particle in a Poiseuille flow. The fixed particle boundary condition is examined in light of other experimental and simulation work. As mentioned in the introduction, both Dhahir & Walters [5] and Carew & Townshend [4] found that cylinders fixed in the streamwise direction in non-Newtonian Poiseuille flow experience a force that is directed toward the wall. We also find this overall qualitative result, with the direction of the cross-stream force for the freely suspended particle opposite that of the fixed particle, as depicted in Figure 3.17. We find that the rotation of the particle does not affect the quantitative force results (up to order $1/(ln(\kappa))$), with the freely rotating particle that is fixed in the streamwise direction feeling the same cross-stream force as the fixed particle that is not allowed to rotate.

In order to find the cross-stream force on a fixed particle in a shear flow, methods previously introduced in the freely suspended particle section will be appropriate. As with the freely suspended particle, it is necessary to have a superposition of an even and odd rate of strain field in order to obtain a net lift force. In the freely suspended particle case, this was achieved from a combination of the shear and quadratic flows. In the fixed particle case, on the other hand, this is achieved

through a combination of the shear flow and the flow due to the relative velocity of the fluid to the particle. The combination of the shear and quadratic flows still gives a net lift force in the fixed particle case; however, the quadratic term is proportional to κ and the relative velocity term is order $1/\kappa$, so as long as κ is small, the contribution due to the quadratic flow is not important. From this scaling, we expect that the cross-stream force on the fixed particle should be order $1/\kappa^2$ larger than that on the freely suspended particle.

The fixed particle analysis includes flow fields due to— 1) a freely suspended particle translating in the streamwise direction in a Poiseuille flow (outlined in Section 3.4.1) and 2) a particle translating in the $-x_1$ direction with a velocity equal to the imposed velocity at a given x_2 (a variation of the solution outlined in Section 3.4.2). The inner solutions for the fixed particle are matched to an outer solution. The flow fields can then be combined to give the overall flow field, from which the cross-stream force acting on the fixed particle can be calculated.

3.5.1 A particle with a streamwise force in Poiseuille flow with variable rotation

Flow relative to the particle

First we consider a particle moving in the x_1 direction with a velocity of the same magnitude as the undisturbed bulk velocity in the Poiseuille flow. This is similar to the previously discussed system (see Section 3.4.2) of a particle translating in the 2 direction. We seek a relationship between the translation velocity and the force on the particle: in this case, the relative velocity of the fluid is equal to the imposed velocity in the overall flow field at the particle position λ. The velocity

and pressure fields take the same form as the inner solution to the translation problem normal to the walls (Equations 3.45 and 3.46)—

$$\bar{u}_{i,inner} = \frac{\bar{F}_j}{4\pi\kappa}\left[\delta_{ij}\left(\ln(r) - \frac{1}{2r^2} + \frac{1}{2}\right) - \frac{x_i x_j}{r^2}\left(1 - \frac{1}{r^2}\right)\right] + \bar{v}_i, \tag{3.63}$$

$$\bar{p}_{i,inner} = -\frac{\bar{F}_i x_i}{2\pi r^2}, \tag{3.64}$$

where the bar denotes a quantity for the problem in which we consider a particle translating parallel to the walls. The above equations are written using the same non-dimensionalization as the perpendicular translation case. The relationship between the force on the particle and the velocity of the undisturbed flow at the particle position is determined in the same way as the force-velocity relationship in the perpendicular translation case, shown in Section 3.4.2. The only difference in the two solutions is that for the parallel translation case, $\bar{F}_i$ is in the 1 direction rather than the 2 direction.

The final relationship between the undisturbed velocity U_1 and the force on the particle in the x_1 direction is similar to Equation 3.59—

$$U_1 = -\frac{\bar{F}_1}{4\pi\kappa}\left[\ln\left(\frac{1}{\kappa}\right) + Z_1\right], \tag{3.65}$$

where

$$\begin{aligned} Z_1 = &- 0.384 - \frac{1}{2}\lim_{\zeta>>1}\ln(\zeta) \\ &+ 2\pi \lim_{\zeta>>1}\int_0^\infty \left[C_1' + D_1' - \frac{1}{2\pi k_1} + \frac{1}{\sqrt{4\pi^2 k_1^2 + \zeta}}\right] dk_1. \end{aligned} \tag{3.66}$$

Figure 3.18 shows Z_1 as a function of λ.

FEM simulations similar to those described in the freely suspended particle case are performed in order to validate Equation 3.65 by specifying a constant fluid

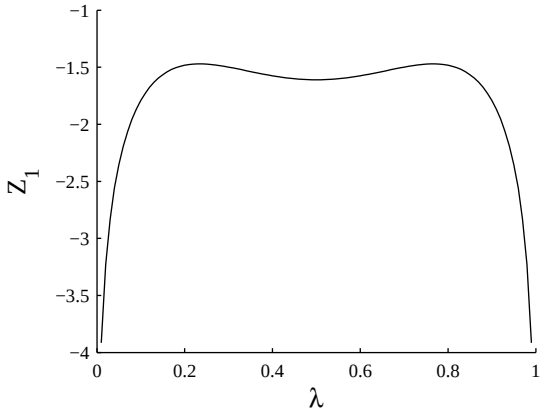

Figure 3.18: Dependence of Z_1 on particle position in the channel.

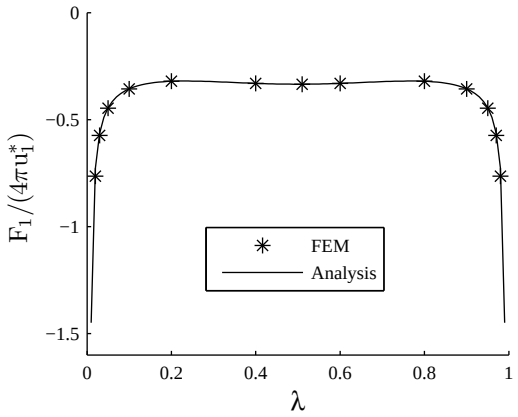

Figure 3.19: Comparison of force between simulation and analysis due to flow relative to the particle. κ=0.01.

velocity boundary condition in the x_1 direction on the particle surface. Again, the particle is fixed in place, and the force due to the fluid motion is calculated, which is valid because of the quasi-steady nature of Stokes Newtonian flow. Figure 3.19 shows good agreement for all values of λ, validating the analytical expression and the simulation results. The force that opposes the particle translation increases dramatically near the walls but is fairly constant elsewhere.

Relevant to the overall velocity field calculation, due to the relative velocity

of the fluid to the particle, an additional contribution to the velocity gradient arises for particles that are not positioned at the channel center. The outer flow has a velocity gradient as the inner region is approached. In order to find this velocity gradient, the matching solution is subtracted from the outer solution, thus removing the singular (and non-contributing) part of the velocity field—

$$\begin{aligned}\tilde{u_1'} =& \tilde{u_1}^{outer} - \tilde{u_1}^{matching} \\ =&(C_1' - A'i\,\mathrm{sgn}(k_1)x_2)exp(-2\pi|k_1|x_2) \\ &+ (D_1' + B'isgn(k_1)x_2)exp(2\pi|k_1|x_2),\end{aligned} \tag{3.67}$$

where u_1' is the non-singular outer solution. A', B', C_1', and D_1' are found in a similar manner as in the problem of the particle translating in the cross stream direction. Next, the derivative with respect to x_2 is found and then the Fourier transform is inverted for $x_1 = x_2 = 0$—

$$\frac{du_1'}{dx_2} = \int_{-\infty}^{\infty} dk_1[-2\pi|k_1|C_1' - A'isgn(k_1) + 2\pi|k_1|D_1' + B'i\,\mathrm{sgn}(k_1)]. \tag{3.68}$$

This velocity gradient contribution is added to the shear flow-induced velocity gradient to give the overall velocity gradient in the 12 direction and calculate the cross-stream force correctly.

Shear flow

Next, we consider the general case of a particle in shear flow that is allowed to rotate at a different speed than a freely rotating particle. For this case, The inner solution velocity field u_i determined in Section 3.4.1 must be modified by adding a perturbation due to the different rotation rate, yielding an extra term equal to $-\frac{1}{r^2}(\Omega_{ij} - \epsilon_{ijk} \cdot \omega_k)$. Otherwise, the velocity and pressure fields are the same as the previous results for the freely suspended particle (see Equations 3.14, 3.15 and 3.16).

Cross-stream force

We sum the velocities and pressures for the relative velocity and particle in shear flow formulations to find the overall flow field. With this determined, the cross-stream force can be found by integrating the second-order fluid stress over the particle surface area in the same manner as is done in Section 3.4.1. The end result for the x_2 force on the fixed particle is

$$F_2 = \frac{-8De\left(4\left(\frac{1}{2}-\lambda\right)+\frac{3}{2}\frac{du_1'}{dx_2}\right)(1-4(\frac{1}{2}-\lambda)^2)\pi}{\left(\ln\left(\frac{1}{\kappa}\right)+Z_1\right)}, \tag{3.69}$$

where the velocity gradient du_1'/dx_2 due to the relative motion of the particle to the walls is given by Equation 3.68 and the non-dimensionalization is the same as for the cross-stream force on the freely suspended particle. The force on the fixed particle is in the opposite direction of the force on the freely suspended particle (cf. Equation 3.27), indicating that the fixed particle experiences a force toward the walls of the channel. From an overall perspective, the reason for the switch in the direction of the cross-stream force is because the overall velocity and velocity gradient fields are significantly altered. The higher velocity gradient is at the near-center side rather than the near-wall side, as is the case in the freely suspended particle. This switch is due to the fact that the cross-stream force on a fixed particle arises from the relative velocity of the fluid to the particle, rather than the gradient of the imposed flow shear rate. Another difference in the two forces discussed earlier is that the cross-stream force arises from the coupling between the linear shear flow and the x_1 relative fluid velocity, since the scaling shows that this is the dominant contribution to the force.

To determine the individual contributions to the cross-stream force on a fixed particle, we can write the velocity field in cylindrical coordinates—

$$u_\theta^{SS} = y\left(4E_{12}cos(2\theta) - \frac{F_1 sin(\theta)}{2\pi\kappa}\right). \tag{3.70}$$

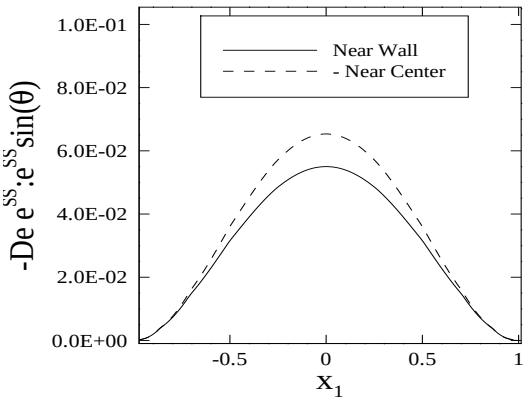

Figure 3.20: Pressure contribution to F_2 on the surface of a fixed particle: $\boldsymbol{e} : \boldsymbol{e}$. $\kappa = 0.0167$, $De = 0.0001$, $\lambda = 0.416667$.

There is no additional contribution to the cross-stream force for a particle that is rotating, and thus the solid body rotation is not included. Hence, the only possible contributions to the cross-stream force could come from the rate of strain tensor and the non-Newtonian pressure, since the convection terms must be zero. In fact, the rate of strain tensor provides a contribution proportional only to the second normal stress difference coefficient, which is exactly canceled by part of the deformation term in the non-Newtonian pressure. The third term from the second-order fluid pressure (Equation 3.10) is the only contributing part of the non-rotating terms to the particle cross-stream force. In order to calculate it, the expression for the rate of strain tensor must be found, with the velocity gradient including Equation 3.68 and the velocity gradient of Equation 3.70. The contribution to the cross-stream force arises from the deformation of the fluid due to the shear stress around the particle. Figure 3.20 shows that there are unequal contributions to the force from the near-center and near-wall sides of the cylinder, yielding a net force toward the wall. Physically, the particle has a higher shear rate on the near-center half of the particle that arises from the combination of the relative velocity and shear flows. Using the same hoop stress argument as in the

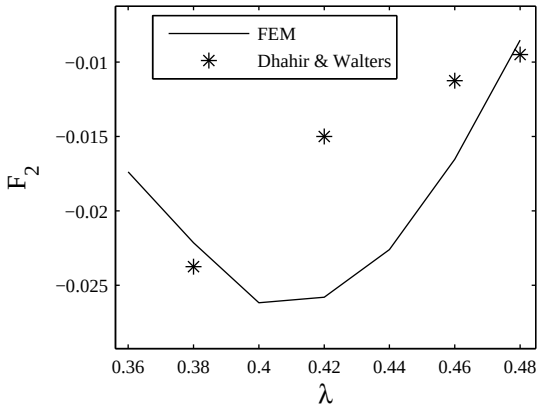

Figure 3.21: Comparison to Dhahir & Walters [5] experiments. $De = 0.865$, $\kappa = 0.3$, $\beta = 0.75$.

freely suspended particle, the particle has an imbalance in the normal forces, with a larger near-center contribution due to the fact that the polymer is more highly stretched on the near-center side.

In the appropriate limits of low De, small κ, and λ far from the wall, the analytical and simulation results for the fixed, non-rotating particle match each other, as can be seen in Figures 3.22, 3.24, 3.26, and 3.25.

Comparison to experiments

Fixed, rotating particle FEM simulation results at the conditions for the Boger fluid studied by Dhahir & Walters [5] are compared to their experimental results in Figure 3.21. Dhahir & Walters specify a flow rate for their experiments; this flow rate was matched in the simulations in a periodic cell of length 480 by iteration. The data do not agree very well, but all data points are within a factor of two between the simulation and experiment. In the simulations, as the particle moves closer to the wall, at first the difference in velocity gradient between the two sides of the cylinder increases, causing a larger force due to the inhomogeneous stretching

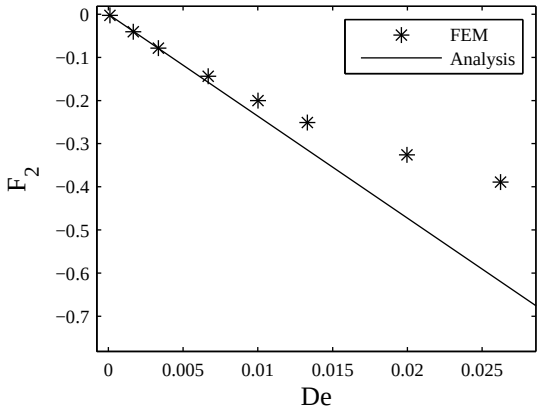

Figure 3.22: Cross-stream force dependence on De for a fixed, non-rotating particle. $\kappa = 0.01667$, $\lambda = 0.4167$, $\beta = 0.85$.

of the polymers near the particle surface. However, as the cylinder gets even closer to the wall, very little fluid flows through the small gap and the rotation velocity of the cylinder. In addition, the velocity gradients on the two surfaces decreases, and the cross-stream force decreases with increasing ϵ. It is uncertain why the experimental results do not show the same behavior as the cylinder approached the wall, but one possible explanation for the discrepancy is the three dimensional nature of the flow in the experimental channel, which had a height to width ratio of 1:1.

De effect

The results of the FEM simulations performed at low De match those of the second-order fluid analysis, but begin diverging at $De > 0.01$, as seen in Figure 3.22. The onset of deviation from analytical results for the fixed particle occurs at a much lower De than is seen in the freely suspended particle (cf. Figure 3.7). This behavior is expected since the shear rate is significantly higher on the surface of a fixed particle due to the relative velocity of the fluid to the particle. Hence,

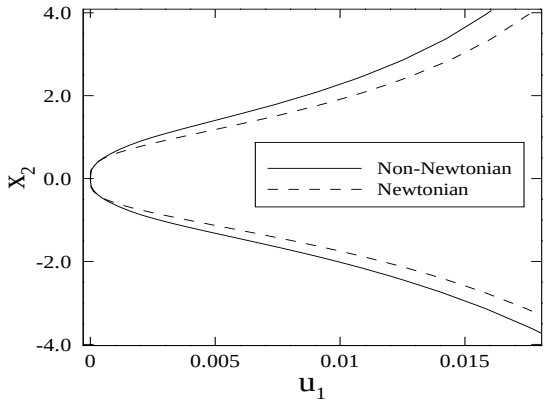

Figure 3.23: Comparison of velocity profiles near a fixed, non-rotating particle for Newtonian and non-Newtonian flows. κ=0.01667, $x_1 = 1$; $De = 0.0263$ and $\beta = 0.85$ for non-Newtonian curve.

for the fixed particle case, a second characteristic flow time U_{max}/a based on the particle radius could be defined in addition to the undisturbed characteristic flow time U_{max}/H based on the channel height. Both of these characteristic flow times are important, since the cross-stream force is derived from a coupling of the shear flow and relative velocity of the particle. Thus, we would expect that De be much less than 1 for the second-order fluid analysis of the shear flow to be valid, and De be much less than κ for the analysis of the relative velocity flow field to be valid.

The finite De deviations from the analytical predictions of the velocity field itself are much higher for the fixed particle case than for the freely suspended particle case. These flow field modifications are shown for $De = 0.0263$ in Figure 3.23, where Newtonian and non-Newtonian velocity fields with the same geometry and pressure gradient are plotted. The velocity gradient field also changes at higher De, becoming smaller than the analytical predictions. This change yields a smaller fluid deformation, which in turn stretches the polymers near the particle to a degree lower than would be predicted. The result is then a smaller cross-stream force than that which would be predicted by the second-order fluid analysis. In

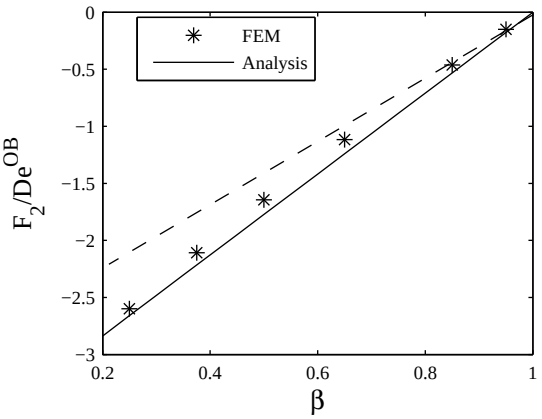

Figure 3.24: Cross-stream force dependence on the ratio of solvent viscosity to zero shear rate viscosity (β) for a fixed, non-rotating particle. $De^{OB} = 0.062$, $\lambda = 0.4167$, $\kappa = 0.01667$.

addition to the changes in the velocity and velocity gradient fields, the longer relaxation time shifts the stress and non-Newtonian pressure downstream, so they do not peak at the center of the particle as in the case for very small De.

Polymer concentration effect

In the limit of low polymer concentration and low De, the analytical and simulation results match. However, as the polymer concentration increases (or β decreases), the cross-stream force deviates from the analytical predictions due to higher order De effects and coupling between the polymer stress field and the velocity field, as shown in Figure 3.24. As with the freely suspended particle, a dashed line is included in Figure 3.24 to differentiate two types of deviation from analytical predictions. First, there is a deviation due to the O(De^2) effects arising due to the finite De^{OB} used in the comparison, which gives a change in the slope of the F_2/De^{OB} vs. β line. As the polymer concentration increases (and β decreases), there is a second deviation due to the change in the velocity field (and hence stress

field) and thus gives a different cross-stream force on the particle than would be predicted.

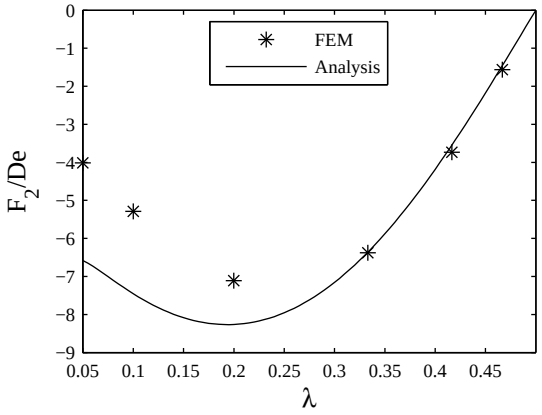

Figure 3.25: Cross-stream force dependence on cross-stream position for a fixed, non-rotating particle. $\kappa = 0.01667$, $\beta = 0.85$.

Particle position

Figure 3.25 shows the relationship between the position λ of the particle and the cross-stream force. The analysis is valid in the limit when the particle is not close to the wall. Unlike the freely suspended particle, the fixed particle does not experience a diverging lubrication force near the wall due to the zero velocity surface boundary condition. The shear rate in the gap does become larger as the gap becomes smaller, but it does not blow up. Rather, the cross-stream force reaches a maximum at about $\lambda = 0.2$, where the difference between the near-center and near-wall shear rates is maximum. As the particle nears the wall, its hydrodynamic interaction with the wall alters the velocity field such that the velocity gradient on both sides of the particle is smaller than analytically predicted, yielding negative deviations in the magnitude of the cross-stream force.

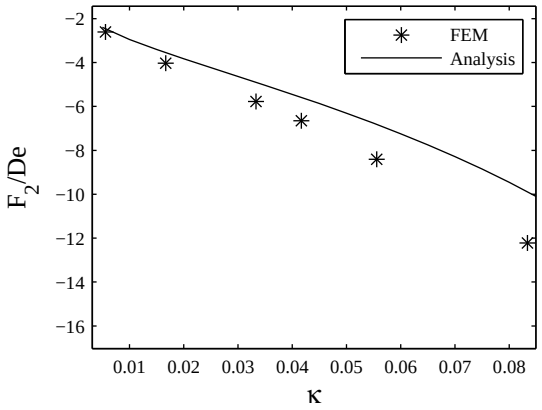

Figure 3.26: Cross-stream force dependence on particle size for a fixed, non-rotating particle. $\lambda = 0.4167$, $\beta = 0.85$.

Particle size effect

The perturbation analysis requires a small particle radius, and Figure 3.26 shows the deviation from this assumption at larger particle radii. As with the freely suspended particle, deviations from the analysis occur because the particle size is large enough to allow the hydrodynamic reflections off of the channel walls to become non-negligible and give an additional contribution to the cross-stream force on the particle.

3.5.2 Freely Suspended and Fixed particles: Discussion

Simulations by Huang et al. [7] indicated that sufficiently large freely suspended cylindrical particles migrate toward the wall rather than the center of a channel in a Poiseuille flow. However, a notable difference between their study and the present study is the boundary condition used on the particle surface. Huang et al. [7] used a condition in which the cylinder was placed in a Poiseuille flow; then, they solved

Newton's equations of motion, calculating the particle motion based on the stress on the exterior of the cylinder. At the initial condition, the particle was stationary, and based on the present study, it should have experienced a cross-stream force pointing toward the wall due to the relative motion of the fluid to the particle. In our analyses and simulations, we find that the cross-stream force arising from the coupling of the relative velocity and the linear part of the Poiseuille flow is order $1/(\kappa^2 ln(\kappa))$ larger than the force arising from the linear and quadratic parts of the Poiseuille flow (compare, e. g. Figures 3.7 and 3.22), and thus a cylinder that has a stationary initial condition will not necessarily have the time required to eliminate the transient effects before reaching the wall. While it is possible that the approach of Huang et al. [7] would have eventually yielded migration toward the center of the channel, the simulations were stopped when the particle reached the wall. Thus, the transient effects built into the study likely do not allow the particle to migrate to the final location that it would have reached if it were to have been at steady state in the beginning. In addition, Huang et al. [7] kept an inertial term ($\partial u/\partial t$) in their $Re = 0$ calculation. Even if the transient effects were eliminated, the non-transient cross-stream force would be balanced by this inertia, giving another reason for the direction of migration to be the opposite to the direction observed in the present study.

3.6 Conclusions

Migration of a freely suspended particle in a creeping Poiseuille flow in a second-order fluid is toward the center of the channel regardless of De, polymer concentration, particle size or initial location. The cross-stream force that produces particle migration occurs due to the inhomogeneous polymer stress in a Poiseuille flow, with

contributions from the convection of the Newtonian pressure, the deformation of the fluid, and the convection of the rate of strain tensor.

Relaxing the conditions necessary to solve the perturbation analysis and extending these results with FEM simulations for an Oldroyd-B fluid shows that higher De, higher polymer concentration, larger particle size, and particles nearer to the wall all will experience forces that are greater than those that would be predicted by the perturbation analysis expanded to order De. Closer to the wall and/or for larger particles, the hydrodynamic reflection of the particle with the wall contributes to the migration of the particle toward the center plane. Very close to the wall, the lubrication flow leads to a diverging non-Newtonian cross-stream force on the particle although the Newtonian normal motion lubrication force maintains a small migration velocity. Finite element simulations confirm the accuracy of the asymptotic analysis for Deborah numbers less than about 0.5 and reveal modifications of the analytical predictions of migration force and fluid velocity with increasing De and polymer concentration.

The cross-stream force on a fixed particle in the same system points toward the wall. In this case, the relative motion of the fluid to the fixed particle significantly changes the undisturbed velocity field and causes the shear rate to be greater on the near-center side of the particle, which in turn increases the polymer stress on that side of the particle. The dominant contribution to the cross-stream force is the deformation of the fluid, which is much higher in the fixed particle case than in the freely suspended particle case. At larger particle sizes and higher De, the fixed particle has a smaller cross-stream force than predicted by the theory.

The previously posited idea by Huang and coworkers [7] that the migration direction for a freely suspended particle is based on the size of the particle, with

a critical size causing a flip in the migration direction, is refuted. The direction of the cross-stream force is found to be a function of the boundary condition on the particle surface rather than a property of the particle.

REFERENCES

[1] F. P. T. Baaijens, H. P. W. Baaijens, G. W. M. Peters, and H. E. H. Meijer. An experimental and numerical investigation of a viscoelastic flow around a cylinder. *J. Rheol.*, 38(2):173–203, 1994.

[2] E.B. Becker, G.F. Carey, and J.T Oden. *Finite Elements*, volume 1. Prentice Hall, 1981.

[3] R.B. Bird, R.C. Armstrong, and O. Hassager. *Dynamics of Polymeric Liquids*, volume 1. John Wiley & Sons, 2nd edition, 1987.

[4] E.O.A. Carew and P. Townsend. Slow visco-elastic flow past a cylinder in a rectangular channel. *Rheol. Acta*, 30:58–64, 1991.

[5] S.A. Dhahir and K. Walters. On non-Newtonian flow past a cylinder in a confined flow. *J. Rheol.*, 33:781–804, 1989.

[6] B.P. Ho and L.G. Leal. Migration of rigid spheres in two-dimensional unidirectional shear flow of a second-order fluid. *J. Fluid Mech.*, 76:783–799, 1976.

[7] P. Huang, J. Feng, H. Hu, and D. Joseph. Direct simulation of the motion of solid particles in Couette and Poisseiulle flows of viscoelastic fluids. *J. Fluid Mech.*, 343:73–94, 1997.

[8] T.J.R. Hughes. *The Finite Element Method: Linear Static and Dynamic Finite Element Analysis*. Dover Publications, 2000.

[9] D.J. Jeffrey and Y. Onishi. The slow motion of a cylinder next to a plane wall. *Quart. J. Mech. and App. Math.*, pages 129–137, 1980.

[10] M.A. Jefri and A.H. Zahed. Elastic and viscous effects on particle migration in plane-Poiseuille flow. *J. Rheol.*, 33:691–708, 1989.

[11] A. Karnis and S.G. Mason. Particle motions in sheared suspensions. *Trans. Soc. Rheol.*, 10:571–592, 1966.

[12] A.W. Liu, D.E. Bornside, R.C. Armstrong, and R.A. Brown. Viscoelastic flow of polymer solutions around a periodic, linear array of cylinders: Comparisons of predictions for microstructure and flow fields. *J. Non-Newt. Fluid Mech.*, 77:153–190, 1998.

[13] C. R. Robertson and A. Acrivos. Low reynolds number shear flow past a rotating circular cylinder. part 1. momentum transfer. *J. Fluid Mech.*, 40:685–704, 1970.

[14] R.L. Schiek and E.S. G. Shaqfeh. Cross migration of slender Brownian fibres in plane Poiseuille flow. *J. Fluid Mech.*, 332:23–39, 1997.

[15] M.D. Smith. *Simulation of Nonisothermal and Time-Dependent viscoelastic flows*. PhD thesis, M.I.T., 2000.

[16] G. Subramanian and D. L. Koch. Inertial effects on the transfer of heat or mass from neutrally buoyant spheres in linear velocity fields. *Phys. Fluids*, 18, 2006.

[17] G. Subramanian and D. L. Koch. Heat transfer from a neutrally buoyant sphere in a second-order fluid. *J. Non-Newt. Fluid Mech.*, 144:49, 2007.

[18] M.A. Tehrani. An experimental study of particle migration in pipe flow of viscoelastic fluids. *J. Rheol.*, 40(6):1057–77, 1996.

[19] M. Zurita-Gotor, J. Blawzsziewicz, and E. Wajnryb. Swapping trajectories: A new wall-induced cross-streamline particle migration mechanism in a dilute suspension of spheres. *J. Fluid Mech.*, page 447, 2007.